Benchmarking OLTARIS For Deep Space Dose Analyses Using MCNP6

By

John Daniel Baunach

Thesis

Submitted to the Faculty of the

Graduate School of Vanderbilt University

in partial fulfillment of the requirements

for the degree of

MASTER OF SCIENCE

in

Physics

May, 2015

Nashville, Tennessee

Approved:

Michael G. Stabin, Ph.D.
Todd E. Peterson, Ph.D.

ACKNOWLEDGEMENTS

I much first acknowledge the Nuclear Regulatory Commission, for without their Nuclear Education Grant Program I would not have had the chance to follow this research wherever it led. This opportunity for graduate-level research is something I never expected to have, so on behalf of all students who are supported by these funds -- thank you.

An immeasurable debt of gratitude is owed to my advisor, Dr. Michael Stabin. His endless patience in teaching the most stubborn and frustrating of students is an inspiration as a person, as a teacher, and as an aspiring health physicist. The lessons I have learned under his tutelage far exceed any mere memorization of facts, and have taught me to expect a high standard in my own research and professional relationships. For this and much more -- thank you.

Much debt is also owed to Dr. Robert Singleterry of NASA's Langley Research Center. I could not ask for a more knowledgeable guide for the content of this thesis, and for impressing on me the true challenges of any potential interplanetary spaceflight. For allowing this student to even be in the room with professionals I have looked up to my entire life -- thank you.

Finally, to the family and friends who have supported me financially, emotionally, and spiritually during my studies at Vanderbilt. Of all these, a special thanks is owed to my parents, who have sacrificed much so that I could be here. Thank you.

TABLE OF CONTENTS

Page

LIST OF TABLES

Table

LIST OF FIGURES

Figure Page

CHAPTER 1

MOTIVATION

Over five decades after the beginning of the human exploration of space, many national space agencies are looking beyond low-Earth orbit with the ultimate goal of establishing a human presence on other worlds. To succeed in this, astronauts and scientists must solve new problems and overcome unfamiliar hazards.

One of these is the radiation environment of space itself. When combined with the long duration of spaceflight and the lack of atmospheric and geomagnetic shielding, this deep space radiation becomes a potentially fatal hazard. To date, every astronaut has returned to Earth relatively unscathed by the effects of radiation (Cucinotta 2001); one reason for this is that with earth's geomagnetic field, having protection from all but the most dangerous bursts of solar particles is considered an acceptable risk for such short flights. However, shielding design *must* be a consideration for any long-term space mission, when natural protections are minimized. In very short order, cosmic background radiation becomes a pernicious threat to human safety on long-range spaceflights.[1]

In determining what level of risk is acceptable, NASA has adopted the policy of a 3% REID (**R**adiation **E**xposure **I**nduced **D**eath) risk level for every astronaut on any mission (see Chapter 2). To fulfill this mandate, NASA must simulate the radiation environments of space to estimate the dose an astronaut will receive. One method uses OLTARIS – the **O**n-**L**ine **T**ool for the **A**ssessment of **R**adiation **I**n **S**pace -- a program developed by NASA at the Langley Research Center in Hampton, Virginia. The OLTARIS program, accessible through any Internet browser, takes user-defined boundary conditions and utilizes the radiation transport code HZETRN to calculate the effects of space radiation on materials and tissues (OLTARIS). To calculate the equivalent dose to a human body, OLTARIS transports particles from a chosen radiation environment (e.g., a solar particle event, a historical background radiation profile, or the radiation profiles of certain planets and moons), through a voxelized human phantom adapted for the program. The user may elect to shield the phantom with any number of materials, in order to estimate the effect that shielding may have on total exposure.

Although some scenarios in Low-Earth Orbit, within the protection of the geomagnetic field, have been sufficiently verified and validated through dosimeters with the astronauts aboard the International Space Station, other scenarios in OLTARIS have yet to be validated (Wilson 1995). The HZETRN user manual states on page 31 that

"Ideally, validation should be accomplished with detailed transport data, obtained from carefully planned and controlled experiments; unfortunately, such data are scarce. ... Although limited

[1] If an astronaut traveling to Mars and back (at shortest, a sixth month journey each way), and stays on the surface for eighteen months, the total exposure would be approximately 1,000 mSv (NASA EP-08). This does not include any radiation dose from a possible exposure to an SPE during the journey - which would expose the astronaut to as much equivalent dose in fifteen minutes as over the rest of the entire mission.

quantities of HZE dosimetry measurements from manned space missions (e.g., Skylab) are available, numerous assumptions... must be made to estimate astronaut dose...
Because many of these assumptions may involve inherently great uncertainties (i.e., factors of 2 or greater), differences in results are difficult to attribute to the particular assumptions or approximations that may have been used in the analysis. *Without definitive GCR transport measurements with which to compare code predictions, other methods of validation must be considered. One such method is to compare HZETRN with limited available proton transport Monte Carlo results."*

In this study, doses calculated through OLTARIS for several exposure scenarios are compared with similar scenarios created within MCNP6 (Monte Carlo N-Particle, version 6), a well-validated probabilistic radiation transport code managed by Los Alamos National Laboratory. As noted above, the ideal validation for OLTARIS – "detailed transport data obtained from carefully planned and controlled experiments" (Wilson 1995) – is, for all practical purposes, untenable. In lieu of the proper *in situ* experimental data, this paper presents a validation approach using MCNP6, the first MCNP code capable of transporting exotic particles while simultaneously handling a voxel phantom.

Because of the fairly simplistic (one-dimensional) treatment of the transport geometry by OLTARIS, the run time of the program is kept low; this is ideal for engineers who, when determining the amount of radiation shielding necessary for a mission, might test a dozen or more iterations of the same vehicle, with only slight optimization adjustments, during the design process. Since this is only an approximation of reality, the more ``life-like'' three-dimensional geometry from MCNP6 is desirable when considering verification of these dose calculations; however, the runtime of MCNP6 is significantly longer than OLTARIS.

This paper seeks to provide a ``sense'' of the accuracy of the OLTARIS calculations, by mimicking and running very simple OLTARIS scenarios in MCNP6. This benchmarking method, if interpreted correctly, could allow OLTARIS users to preserve the runtime advantage of OLTARIS without forsaking all certainty in its results.

CHAPTER 2

TECHNICAL INTRODUCTION

Radiation in Space

Radiation in space comes from many sources, from both inside and outside of the solar system. In **deep space** (or **free-space**) -- i.e., far away from any planetary surfaces, atmospheres or magnetospheres -- two primary sources of radiation, in addition to the ubiquitous solar wind, are **galactic cosmic rays** (**GCRs**) and energetic **solar particle events** (**SPEs**).[2]

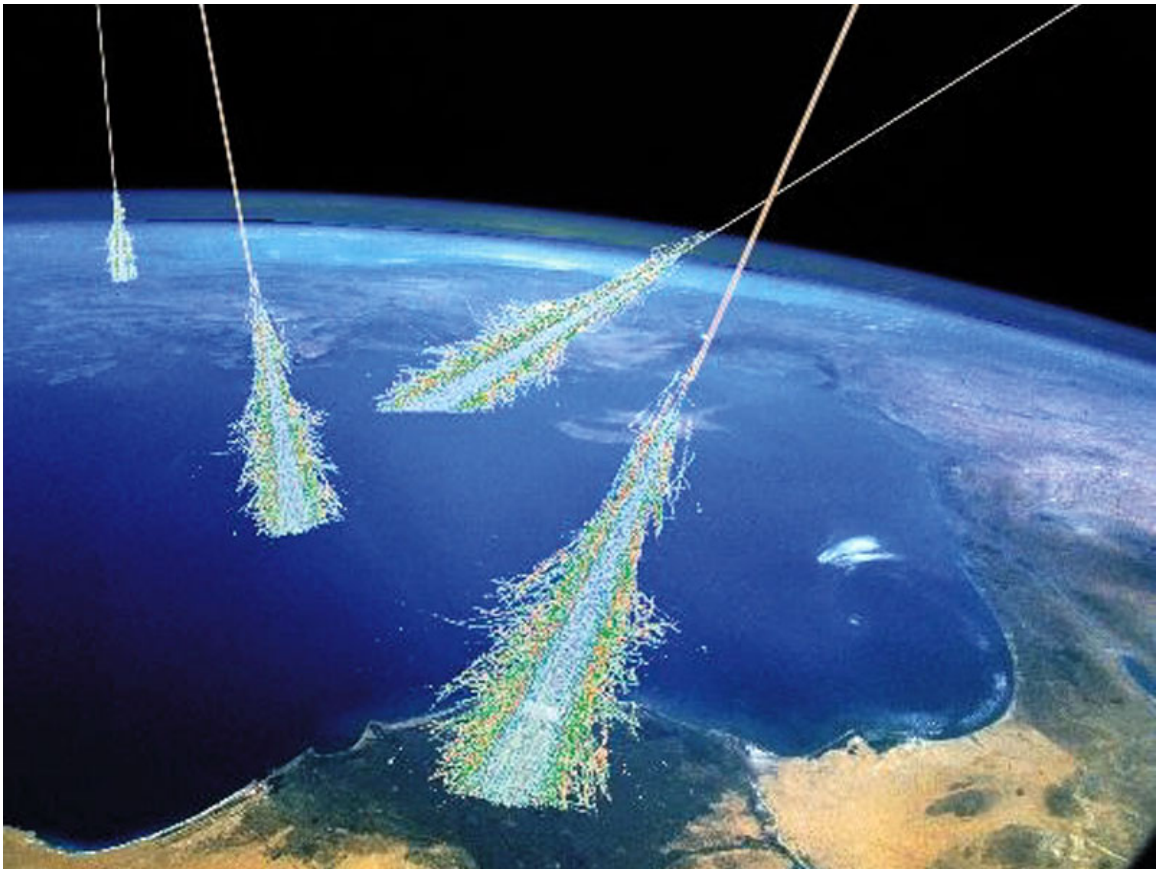

Figure 2.1 - A depiction of galactic cosmic rays hitting the Earth's atmosphere (*Credit: Simon Swordy, U. Chicago.*)

[2] Both of these acronyms - GCR and SPE - have dual meanings. GCR sometimes refers to *galactic cosmic* ***radiation***, and SPE can also be an acronym for *solar* ***proton*** *event*. Many authors use these acronyms interchangeably, but this paper will use the primary extensions – *galactic cosmic ray* and *solar particle event* – throughout to avoid any confusion.

Galactic Cosmic Rays

Galactic cosmic rays (**GCRs**) are narrow beams of high-energy particles that originate outside the solar system, but generally from within the Milky Way Galaxy. Their exact source is still unknown, but there is wide agreement among astronomers that they are emanations from either active galactic nuclei and/or supernova remnants (Ackermann 2013). They consist almost entirely of ionized atomic nuclei (about 99%); of these, it is about 90% **free protons** ($^{1}H^{+1}$), 9% **alpha particles** ($^{4}He^{+2}$), and the rest high-energy ionized nuclei of elements between lithium and uranium (**HZE ions**). The remainder is a trace amount of **beta-minus particles** (high-energy solitary electrons) and occasionally some anti-matter.

GCRs are characterized by their particles' extremely large kinetic energies. The energy of an average GCR particle is 0.3 GeV, but particle kinetic energies have been recorded as high as 300 EeV (Bird 95). Due to these high energies, a GCR is a very penetrating radiation particle. Thin to moderate shielding is effective in reducing radiation dose to humans, but, interestingly, shield effectiveness will actually drop as thickness increases -- the production of a large number of secondary products, including neutrons, from nuclear interactions between GCR particles and shield nuclei yields diminishing returns with each additional layer of shielding (Johnson 1993).

Total GCR flux into the solar system is constant (Figure 2.2), but it is modulated by the solar activity cycle. During maximum solar activity, the interplanetary solar magnetic field does not appreciably reduce the number of higher energy GCR particles, but lower energy particle fluence is significantly curtailed as the strengthened magnetic field acts as a radiation shield for the inner planets. The intensity of GCRs detected near Earth during solar maximum is attenuated by a factor of approximately 2.5, compared to GCR intensity at solar minimum (Johnson 1993).

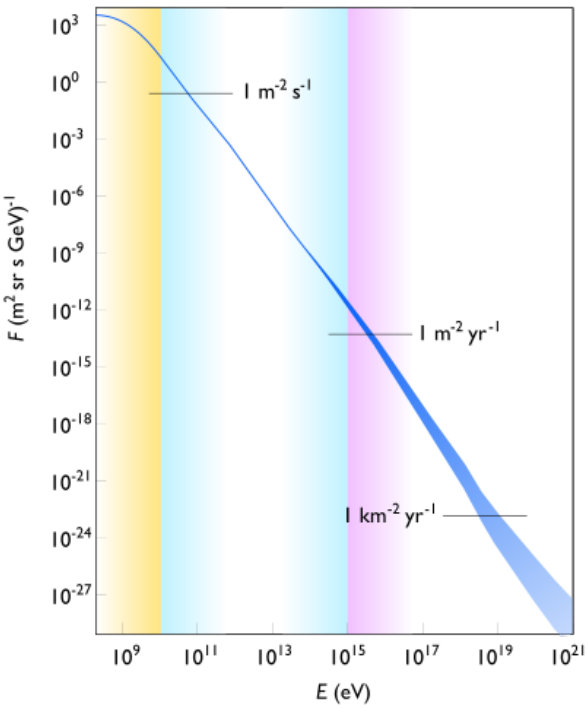

Figure 2.2 - Cosmic Ray Flux vs. Particle Energy
(*Credit: Sven Lafebre*)

When a GCR collides with the Earth's atmosphere, the particles interact with molecules in the upper ozone to produce cascades of lighter particles -- typically neutrons and charged mesons (like pions and kaons). Some of these mesons subsequently decay into muons, which are able to reach the Earth's surface. As a result of these secondary cascades, GCRs account for approximately 16.25% of the world-averaged natural background radiation (UNSCEAR 2008).

The Solar Wind

The solar wind is a constant supply of particles that is released from the Sun in all directions. It is mostly ionized protons and electrons (Kallenrode 2004), with energies in the range of 1-10 keV (Fig. 2.5). The energy of particles in the solar wind are much lower than those in GCRs, but as the solar wind just as ubiquitous it should still be considered an integral part of the local space radiation environment.

The solar wind has two major components: the slow solar wind and the fast solar wind. The slow solar wind moves at about 400 km/s, while the fast moves at about 750 km/s (Feldman 2005). The slow solar wind is a denser, more variable particle stream, and closely matches the composition of the solar corona; conversely, the fast solar wind's composition is closer to that of the photosphere. While the slow solar wind is thought to originate from the equatorial region of the Sun (Harra 2008), the fast solar wind is believed to pour from coronal holes, concentrations of open magnetic field lines that often appear near the Sun's magnetic poles (Marsch 2005) (Suess 1999).

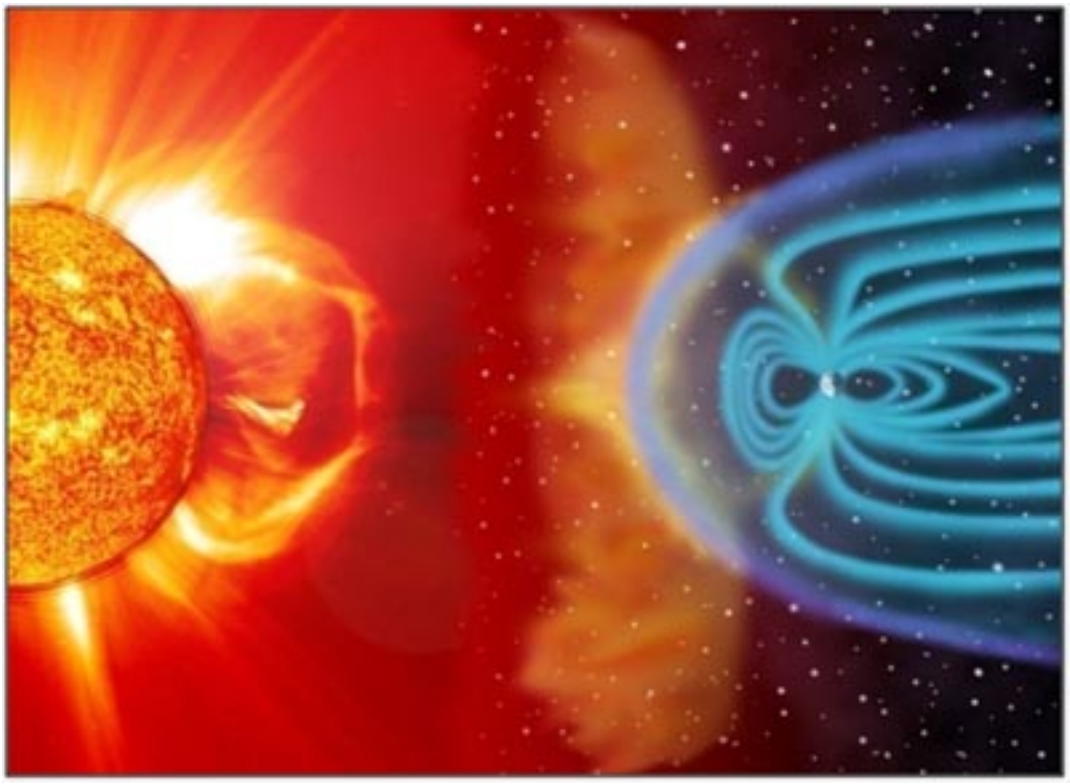

Figure 2.3. A depiction of an SPE interacting with the geomagnetic field of Earth (not to scale) (*Credit: K. Endo, National Geophysical Data Center*)

Solar Particle Events

A **solar particle event** (**SPE**) is an ejection of highly energetic particles from the Sun into the outer solar system. Unlike the omnipresent solar wind, an SPE is typically caused by a seismic event on the surface of the Sun, such as a coronal mass ejection or a solar flare. The event accelerates these solar energetic particles (SEPs) to very high speeds. The composition of any SPE is about 99% free protons, with the rest being alpha particles, trace amounts of ionized high-Z nuclei (HZE ions) and other exotic particles (Williams 98). The composition of SPEs is similar to the composition of the surface of the Sun -- evidence that these particles come from the body of the star itself, and not the corona.

The kinetic energy of a **solar energetic particle** (**SEP**) can vary substantially (usually 1-100 MeV), but kinetic energies in excess of 10 GeV have been recorded (Mewaldt 2005) (Shea 1992). Although they are energetic, most SPEs are relatively short-lived, lasting less than one or two days (Johnson 1993).

While GCRs are a ubiquitous source of radiation, SPEs are intermittent and currently impossible to predict, occurring without much warning. SPEs are also anisotropic; what telescopes in one area of the solar system might see may not be seen in another, and what may affect one part of the solar system may not affect other parts of the solar system evenly or at all.

During periods of maximum solar activity, the frequency and intensity of solar flares -- and thus the intensity of SPEs -- increase. Most flares do not present a significant hazard, because they are either too small to inject significant numbers of energetic solar particles or because they eject particles to other parts of the solar system, away from Earth. According to JSC, however, ``flares or rapid sequences of large flares that are orders of magnitude greater in intensity than most flares, are of particular concern for generating very large energetic SPEs. These solar proton events generally occur only once or twice a solar cycle'' (Johnson 1993).

Other Source of Space Radiation

Although outside the scope of this paper, there are other important sources of radiation that future astronauts will be exposed to when close to any planetary body. Since the overarching goal of this research is the protection of human life, and since future research will likely focus on some or all of these other sources, a brief description of each is warranted.

Albedo Neutrons

Albedo neutrons, as the name suggests, are neutrons that are created by the interaction of high-energy particles (usually from GCRs) with a planetary surface or its upper atmosphere, and then scattered back outwards into space. While these neutrons are not significant far from any celestial bodies, in low planetary orbit they can be a significant dose of radiation.

The albedo neutrons from Earth's atmosphere have been measured since at least the 1960's (Sokolov 1968). The surface of the moon, as well as the surfaces and atmospheres of Mars, also produce albedo neutrons, so any future planning for missions of permanent settlement on these bodies will have to include a closer study of the intensities of these particles.

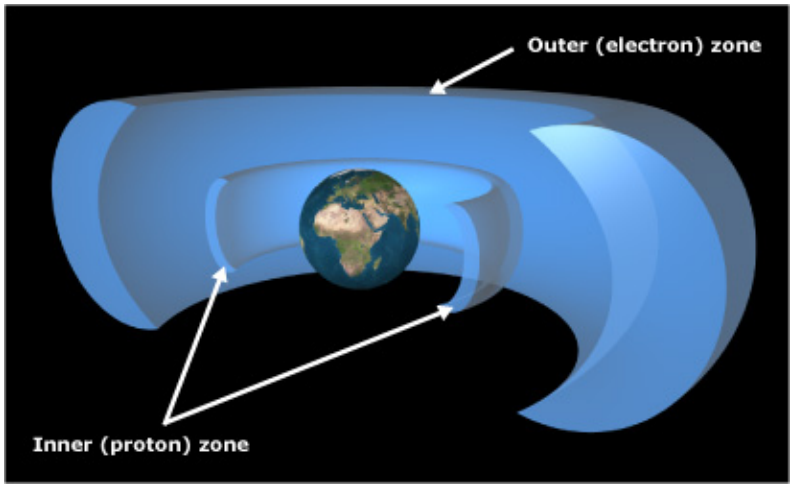

Figure 2.4. The Van Allen belts.
(*Credit: ESA*)

The Van Allen Belts

The Earth's magnetic field is responsible for the formation of the Van Allen belts – two bands of plasma radiation surrounding the Earth. The outer belt is dominated by electrons, while the inner belt is overwhelmingly protons and other ionized nuclei. Since spacecraft leaving Earth's gravitational well might pass through the Van Allen belts, these are collectively an important source of radiation to consider for astronauts venturing into deep space (Van Allen 1958).

Similar radiation belts exist around other bodies with active geomagnetic fields (Bhardwaj 2000). Certainly, any spacecraft entering these fields will be forced to deal with radiation environments similar to Earth's Van Allen belts.

Manmade Sources

Additional environmental hazards may be present from the use of manmade sources. These hazards may be in the form of exposure resulting from medical investigations, radioisotopic power generators, or small sources for experiments. Lunar and Martian missions may include either nuclear reactors for power or propulsion purposes that will contribute to crew radiation health concerns.

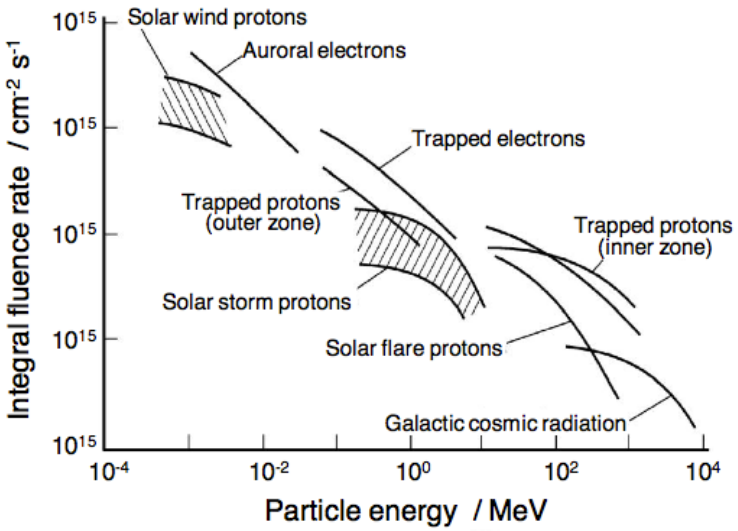

Figure 2.5. The integral fluences and strengths of various space radiation sources. (*Credit: Lisa Simonsen, NASA Langley Research Center.*)

Terrestrial Protection from Space Radiation

Earth's abundance of complex life forms is indebted to both the planet's active magnetic core and its thick atmosphere. These natural phenomena actively protect the earth's surface, and the life forms on and near it, from nearly all cosmic-born radiation.

The Geomagnetic Core

The solar wind is deflected by the earth's magnetic field as it approaches the planet, reflected around a region called the magnetosphere. Most manned spaceflight missions have been conducted in low Earth orbit, all within the protection of this magnetosphere. The geomagnetic field shields crews from large SPEs and a significant portion of GCRs (Johnson 1993). For the LEO missions which have typified the U.S. manned space program, the largest fraction of the radiation exposure received has resulted from passage through a region known as the South Atlantic Anomaly (SAA), with most of the rest coming from GCRs (Johnson 1993). Fortunately, no major solar proton events occurred during the Apollo missions, when astronauts traveled beyond Earth's protection and into possibly lethal situations – this is simply due to fortune, however, more than any foresight or planning, as SPEs cannot be predicted with accuracy.

The Upper Atmosphere

Earth's atmosphere provides a shielding thickness of approximately 1,020 g/cm^2 - about two orders of magnitude times than an average aluminum spaceship (the International Space Station has a thickness of about 10 g/cm^2). Coupled with the geomagnetic field, this is one of the most significant radiation shields that living organisms of Earth have. Only the hardiest microorganisms can survive unshielded in the vacuum of space (Horneck 1994). The relative strength of the atmosphere of Earth reemphasizes the magnitude of the task of providing adequate radiation shielding for humans in deep space.

Monte Carlo Radiation Transport Codes

Physicists in the early twentieth century attempting to describe radioactive phenomena quantitatively were overwhelmed by the enormity of the problem. For the first fifty years after Roentgen, Curie and Bequerel, the computing power necessary to follow the interactions of even a few hundred particles, much less the millions of particles in an SPE or GCR, was far beyond feasible for all but the most important problems. It wasn't until the creation of the Manhattan Project that Stanislaw Ulam, Nick Metropolis, John von Neumann and others produced both a method of computing these quantum interactions, and a computer powerful enough to run these calculations - the ENIAC, one of the first electronic computers (Anderson 1986). This non-deterministic method of calculating radiation transport was the so-called ``Monte Carlo method;'' the name itself was homage to the casino in Monaco, where Ulam's uncle loved to gamble (Metropolis 1987) (Metropolis 1949).

The heart of the Monte Carlo method is the repeated application of probabilistic phenomena through calculations, using pseudorandom numbers to apply ``chance'' to simulated stochastic processes, such as particle scattering or radioactive decay. Doing so repeatedly obtains a numerical result that can accurately model quantum mechanical phenomena, such as the relativistic collisions of particles in radiation environments.

The number of Monte Carlo transport codes in existence today is too numerous to exhaustively list every program, and each varies in their utility to a particular subfield of physics. Codes that receive notable use across a wide number of fields include GEANT, FLUKA, EGSnrc, PHITS, and MCNP; each has advantages in certain situations and for different users.

EGSnrc

EGSnrc (**E**lectron **G**amma **S**hower from the **N**ational **R**esearch **C**ouncil of Canada) is a Monte Carlo code system evolved from the EGS code, developed at the Stanford Linear Accelerator Center in the 1970s by Richard Ford and Walter Ralph Nelson for experimental design. In the 1980s, Dave Rogers of the National Research Council of Canada in Ottawa worked jointly with Nelson and Hideo Hirayama of KEK in Japan to develop EGSnrc for use in the medical physics community (Nelson 1985). EGSnrc improved on the accuracy and precision of the charged particle transport mechanics and the atomic scattering cross-section data used in the latest EGS code, EGS4 (Kawrakow 2000). Today, EGSnrc is referenced in around 30% of all Monte Carlo related publications in the leading journals Medical Physics and Physics in Medicine and Biology, and is used extensively by medical physicists (CA-NRC).

EGSnrc transports electrons, photons and positrons through material, with particle energies ranging from 1 keV to 10 GeV, and uses a C++ geometry library to define its environments and particle sources (CA-NRC). Although a well-benchmarked and reliable code for use in medical physics applications, the narrow range of particles makes modeling the exotic space radiation environment impossible.

FLUKA

FLUKA (FLUktuierende KAskade) is a Monte Carlo software sponsored and copyrighted by the INFN (*Istituto Nazionale di Fisica Nucleare*, or National Institute for Nuclear Physics) and CERN (the European Organization for Nuclear Research, originally the *Conseil Européen pour la Recherche Nucléaire*). The origin of FLUKA is around 1962-1967, when Johannes Ranft of CERN wrote the first high-energy Monte Carlo transport codes to simulate hadron cascades. FLUKA is developed using the FORTRAN language, and is currently around 400,000 lines of base code.

It is accepted that three different generation of "FLUKA" codes can be distinguished by their main authors, from the early 1960's and 70's code (J. Ranft and J. Routti), to that of the 1980's (P. Aarnio, A. Fassò, H.-J. Moehring, J. Ranft, G.R. Stevenson), to the modern version of FLUKA (A. Fassò, A. Ferrari, J. Ranft and P.R. Sala) (FLUKA). While the named has not changed with successive version releases like other Monte Carlo codes (e.g. EGS, GEANT, MCNP), each code generation is considered entirely distinct and improved upon the previous version.

FLUKA has many applications in particle physics, high energy experimental physics and engineering, shielding, detector and telescope design, cosmic ray studies, dosimetry, medical physics, and radiobiology. FLUKA software code is used by Epcard, which is a software program for simulating radiation exposure on airline flights. (Davis 2008). In general, FLUKA is called upon to handle high energy particle interactions: it transports photons, electrons, neutrinos, muons and hadrons - 63 particle types in all, plus a large number of heavy ions - at energies up to 20 TeV, well within the range of the space radiation environment. Its minimum energy cutoff is around 20 MeV for neutrons, after which a table of cross-sections is used (FLUKA).

PHITS

PHITS (Particle and Heavy Ion Transport System) is a general purpose Monte Carlo particle transport simulation code developed by numerous institutions, including JAEA, RIST, and KEK. It can deal with the transport of all particles (including hadrons, leptons and heavy ions) over wide energy ranges, using several nuclear reaction models and nuclear data libraries (PHITS).

GEANT4

GEANT4 is a toolkit for the simulation of the passage of particles through matter (GEANT). Its areas of application include high energy, nuclear and accelerator physics, as well as studies in medical and space science (Agostinelli 2003). GEANT4 can transport neutrons, protons, muons and pions from 250 eV up to 1 TeV (Allison 2006).

MCNP6

Monte Carlo N-Particle, or MCNP, is the descendant of the very first Monte Carlo code programmed by Stanislaw Ulam, John von Neumann and Nicholas Metropolis at Los Alamos during the Manhattan Project, when they were investigating neutron transport. In 1947, Enrico Fermi developed a computer, called FERMIAC, to track neutrons through a material via the Monte Carlo method. Over the next couple of decades, a number of independent Monte Carlo codes appeared, with acronyms like MCN (neutrons), MCS, MCP, and MCG (gammas). In 1977,

MCG and MCN were combined, and the first ``MCNP'' code – Monte Carlo Neutron-Photon – was created (MCNP6-1-0).

The meaning of MCNP changed from ``neutron photon'' to ``N-particle'' when electron transport was introduced to and merged with the existing MCNP program in 1990. By 1996, many more particles had been added, and a patch was made to add the LAHET code to MCNP4B, dubbed the ``Many-Particle MCNP Patch.'' This multi-particle code gained wide acceptance and additional sponsors, so much so that it began to grow as its own distinct code: MCNPX. Meanwhile, drastic upgrades and changes to the MCNP4C code to take advantage of parallel computing and Fortran 90 flexibility resulted in a new generation of MCNP: MCNP5. This code was incompatible with MCNPX, however, and the two codes continued to diverge until recombination efforts by Los Alamos National Laboratory in July 2006. The full release of MCNP6 - the successor to both MCNP5 and MCNPX - occurred nearly a decade later, in 2013 (MCNP6 Beta 2 Manual).

For the purposes of transporting high-energy particles, specifically exotic deep space particles, both the computing capabilities of MCNP5 and the particle transport abilities of MCNPX are needed. For the first time under MCNP6, space radiation can be reasonably modeled in the MCNP environment; and while improvements will continue to be made, the statistical validity of the code is as robust as either MCNP5 or MCNPX, and fully capable of use in estimating space radiation doses.

To use MCNP6, the user creates an input file (called the ``input deck'') that is read by MCNP6. The file contains information about the problem, such as:

- a description of the situation's geometry;
- a description of the situation's materials and cross sections;
- the location and characteristics of the particle source(s);
- the types of answers, or tallies, desired; and
- any variance reduction techniques used to improve efficiency.

A more thorough treatment of MCNP6's input deck is given in Chapter 3 of this paper.

Computational Human Phantoms

Even as the initial Monte Carlo methods were developed and particle transport through basic materials became better understood, a need for more complex calculations became apparent: particle transport through the human body itself, and the modeling of the radiobiological damage in the cells of the body.

The ICRP Sphere

Figure 2.6. An example ICRP 60-inspired ``moderator sphere''.
(*Credit: Berthold*)

The very first human models (``phantoms'') were anything but human shaped; they were simple spheres, with approximately the same density and isotopic composition as human tissue. In the creation of universal regulations for radiation protection, approximating the human body was not feasible or even necessary; because the variance between individuals is (1) too varied to easily model, and yet (2) not varied enough to change the fundamental principles of radiation biophysics, a simple ``standard candle'' would be a sufficient starting point for regulatory cases. When monitoring doses across locations, populations and time, this (reproducible) standard is ideal for uniform area monitoring and evaluation.

For determining all operational quantities for area monitoring, the International Commission on Radiological Protection has adopted just such a simple phantom: the **ICRP sphere** is a sphere of diameter 30 cm, with tissue-equivalent density (1 g/cm^3) and mass composition (76.2% oxygen, 11.1% carbon, 10.1% hydrogen and 2.6% nitrogen). This simple model approximates the human body well, both in terms of composition and in scattering properties, for basic monitoring needs. For dosimetry calculations, however, more than a sphere is needed: creating a human-shaped phantom (approximately) was the next natural step (ICRP 60).

The Cristy-Eckerman Series

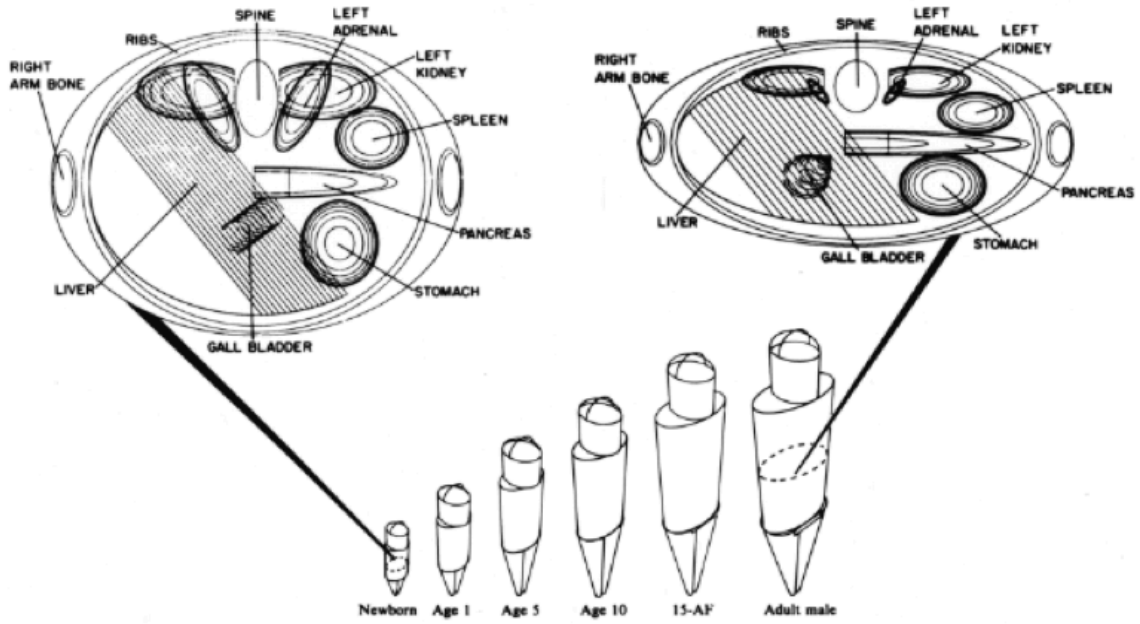

Figure 2.7. The Cristy-Eckerman phantoms.
(*Credit: Cristy 1987)*

Moving beyond simple spheres, Cristy and Eckerman published a report from Oak Ridge National Laboratory in 1987 on their development of an entire ``family'' of human phantoms: a newborn, a 1-year-old, a 5-year-old, a 10-year-old, a 15-year-old/``Adult Female'', and an adult male (Fig. 2.7). These were simple cylindrical and conical shapes, but the represented an important step in the development of human phantoms. For the first time, phantoms attempted to recognize the anatomical differences between people at different ages, as well as different genders. Although there were some irregularities with the Cristy-Eckerman series of phantoms -- e.g., the organs were still vaguely ``ovular'', and the 15-year-old and adult ``males'' had full breasts alongside male anatomical parts for female organ calculations -- they were an important step on the road to image-based phantoms.

Another important and complementary step to Cristy and Eckerman's work was taken eight years later by Michael Stabin and colleagues at Oak Ridge in 1995; the development of an actual female phantom (not merely a hermaphroditic combination of parts placed on the male phantom), and phantoms for pregnant women at the end each trimester of fetal development (Stabin 1995) (RADAR). This development allowed for calculations of radiation dose not only to the mother, but to the fetus itself. Since the occupational limits for declared pregnant women had been significantly altered since the 1982 *United Auto Workers vs. Johnson Controls* Supreme Court case, this was a long-awaited model development, and completed the set of phantoms needed for occupational dosimetry calculations (Dewerd 2014).

Image-Based Phantoms

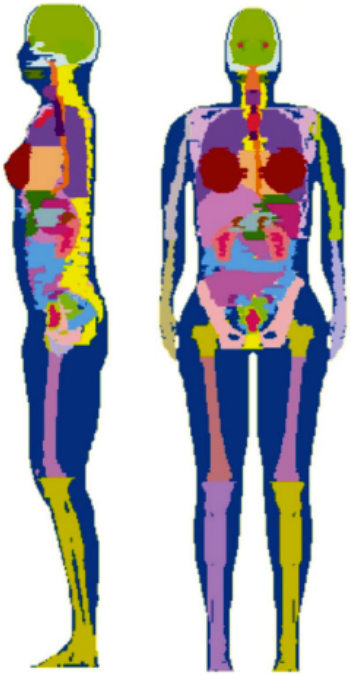

Figure 2.8. The CALDose FAX phantom, with organs and skeletons exposed.
(*Credit: Kramer 2004*)

As computers increased in processing power throughout the late twentieth and early twenty-first century, more and more complex phantoms became available for the computation of dose and equivalent dose in transported radiation environments. Similar advances in medical technology allowed for then-unprecedented high-resolution imaging of the human body. Prime examples of image-based phantoms produced during this time are the MAX05 and FAX05 phantoms from the CALDose team in Recife, Brazil. Each phantom was created from dozens of CT scans on both male and female cadavers, which were processed into a voxelized representation of the body with distance organ identities (Kramer 2006).

Recent advances in imaging techniques and 3D software development have allowed for even more improvements upon these image-based models, leading to the release by the CALDose team a completely new phantom set in 2011 (Kramer 2010) (see MASH & FASH, Chapter 3). As the trend towards higher and higher resolution voxel phantoms continue, the accuracy and individualization of human phantom dosimetry should also be expected to rise. As this occurs, regulations that govern dose limits should be expected to evolve as well, as they have since the beginning of the atomic era.

Radiation Dose Limits

Radiation can cause permanent damage in both biological and electronic systems -- this much is known. On Earth, humans, other life forms, and electronic systems are all protected by the geomagnetic field emanating from the planet's molten metal core, which deflects much of the radiation emanating from the Sun (the ``solar wind'' and the more energetic solar particle events, caused by coronal mass ejections) and from other locations beyond the solar system.

ICRP 103, which was published in 2007 to update the recommendations from the 1990 release, states that *"exceptional cases of cosmic radiation exposures, such as exposure in space travel... should be dealt with separately from the conventional approach of occupational exposure"* (Boettlicher 2008). Because of the high levels of radiation and the many other inherent dangers of space, astronauts are correctly considered distinct from other civilians who work in radiation environments. This distinction is unique; for all other radiation workers, the exposure limit is set not by their employer (NASA) but the federal government, through the arm of the office of Nuclear Regulatory Commission and, previously, the Atomic Energy Commission.

Radiation Dose Limits for NASA Astronauts

Early in NASA's history, radiation was recognized as a hazard to humans traveling into orbit, and crew exposures have been monitored since the Mercury program. Astronauts have been classified as radiation workers by the U.S. government; as such, since Executive Order 12196 (1980), a program is required by OSHA and the NRC for to help reduce astronaut exposure to radiation. Since OSHA does not have standards for spaceflight procedures, NASA is allowed to create parallel regulations if the existing regulations are thought to be too limiting or inappropriate.

The applicable regulations are 29 CFR 1910.96, and NASA has considered these to be, in most cases, too restrictive. Therefore, NASA has sought (and received) permission to create their own standards, which follow six principles (Johnson 1993):

- that their standards' use applies to a limited population
- that they maintain detailed flight crew exposure records
- that they plan pre-flight hazard assessment/appraisal
- that they are active in making planned exposures be kept **A**s **L**ow **A**s **R**easonably **A**chievable (**ALARA**)
- that they maintain operational procedures and flight rules to minimize the chance of excessive exposure, and
- that man-made onboard radiation exposure complies with 29 CFR 1910.96, except where the mission/objectives cannot be accomplished otherwise.

NASA adopted the recommendations within NCRP 89, ``Guidance on Radiation Received in Space Activities,'' giving the basis for their alternate exposure standards, and also in conjunction with ICRP 123 (Dietze 2013). According to Johnson Space Center (Johnson 1993),

*``Whereas monthly and annual limits primarily exist to prevent the short term physiological effects of exposure, career limits exist to contain radiation risk within a **3% increased lifetime cancer mortality.**''*

This requirement is known as **3% REID**, or **"3% Radiation Exposure Induced Death."** The justification for this is the use of comparative risks; the average lifetime risk of accidental death in occupations such as construction, agriculture, and other blue collar jobs lies somewhere between 1.5% and 3%. Other high-risk occupations, like test pilots, exceed 10% in some cases (NCRP 132). In context, NASA's radiation limit is almost conservative (although, of course, there are many other ways that astronauts could experience accidental death).

Former NASA Astronaut Career Limits, by Age and Sex, 1989-2000				
SEX	AGE			
	25	35	45	55
Male	1.50 Sv	2.50 Sv	3.25 Sv	4.00 Sv
Female	1.00 Sv	1.75 Sv	2.50 Sv	3.00 Sv

Table 2.1. Former NASA Career Exposure Limits, 1989-2000

Current NASA Astronaut Career Limits, by Age and Sex, 2000—				
SEX	AGE			
	25	35	45	55
Male	0.7 Sv	1.0 Sv	1.5 Sv	3 Sv
Female	0.4 Sv	0.6 Sv	0.9 Sv	1.7 Sv

Table 2.2. Current NASA Career Exposure Limits, 2000-Present

However, initial recommendations from the NCRP evaluation of new atomic bomb survivor data suggested that even lower career limits for astronauts would be needed to maintain 3% REID (Johnson 1993). In 2000, the NCRP released NCRP Report 132, which superseded the data in NCRP 89 and gave new guidelines for astronaut exposure limits (Table 2). New recommendations require a limit of 50 mSv/year, with a cumulative limit of (age x 10 mSv) after age 18, resulting in an estimated average maximum lifetime risk of fatal cancer of approximately three percent (NCRP 132).

Research Motivation

The motivation for this research, then, is clear. NASA's mandate to protect humans partaking in spaceflight, whether in orbit or beyond to deep space, is at the heart of radiation protection research like this paper.

OLTARIS must have quantifiable uncertainties for its calculations; as engineers looks to quickly test, refine, and optimize their space vehicles, knowing the uncertainties is a necessity for thoughtful and educated design refinement. The first steps for providing this design ``safety net'' in the analysis of OLTARIS results are described in the next chapter.

CHAPTER 3

METHODS

The duplication of six scenarios found in OLTARIS, recreated as faithfully as possible within the confines of the MCNP6 code, is the goal of this research.

The motivation for this is found on page 2 of the OLTARIS user manual – ``The answers that [OLTARIS] give[s] need to be accurate, characterized by an uncertainty, and reproducible... [with] verification, and validation'' (OLTARIS). Although there is little reason to expect calculations from OLTARIS vary wildly from reality, OLTARIS currently does not provide errors analyses or uncertainties to the user along with its final product. MCNP6, however, has robust statistical analyses that can provide a sense of certainty to the calculations, through converted OLTARIS code. Although this is not the original OLTARIS code, a faithful (or near-faithful) recreation in a well-validated code like MCNP6 could provide a basis for expected uncertainty levels in the original OLTARIS calculations; and future, more complex scenarios than those tested here will follow a similar process to discover the uncertainties in those calculations.

There are a number of challenges involved in such a conversion, however; they are outlined below, after a brief overview of each program.

OLTARIS

OLTARIS -- The **O**n-**L**ine **T**ool for the **A**ssessment of **R**adiation **I**n **S**pace -- is the successor to the SIREST program developed in the early 2000's by NASA. Deployed in 2008 and supported at NASA Langley Research Center (NASA LaRC), OLTARIS is a Web-based program that allows engineers and scientists to assess the effects of space radiation environments on humans and electronics while inside spacecraft, spacesuits, habitats, and rovers (OLTARIS).

OLTARIS' architecture divides neatly into two parts: the website interface and the execution environment.

The **website** (https://oltaris.nasa.gov/) is where users interact with OLTARIS, and where they choose mission parameters, define shielding geometry and material thickness distributions, and receive the outputs of the response functions. The website is built with a combination of open source (Ruby on Rails core, MySQL database, Apache server) and licensed (Adobe Flash) components.

The **execution environment** is where all OLTARIS computations are performed. This is hosted on a computer cluster at NASA LaRC, and is ``primarily FORTRAN executables, tied together with some Perl and Ruby scripts.'' Data is passed between the web server and the cluster using XML files. Jobs are managed with the open-source Sun Grid Engine (SGE).

There are five elements a user must define in order for OLTARIS to perform any computation: (1) the **radiation environment** the code must transport, (2) the **material properties** of the object being analyzed by the program, (3) the **geometry** of the object, (4) the method of radiation **transport**, and (5) the desired **response functions** (outputs) that the user wishes to have output to the web interface. Each of these elements has one or more corresponding modules in the OLTARIS program schematic.

Radiation Environment

As of March 2015, the user chooses from eight pre-defined external radiation environments (Fig. 3.1). Each of these radiation environments are modular combinations of GCR, SPE, trapped electrons within a geomagnetic field, trapped protons within a geomagnetic field, and/or albedo neutrons from any nearby atmosphere (OLTARIS).

Two environments are of special interest to this paper – **GCR, Free-Space, 1 AU** and **SPE, Free-Space, 1 AU**. Both of these environments are analogous to deep space, and they are described in more detail below.

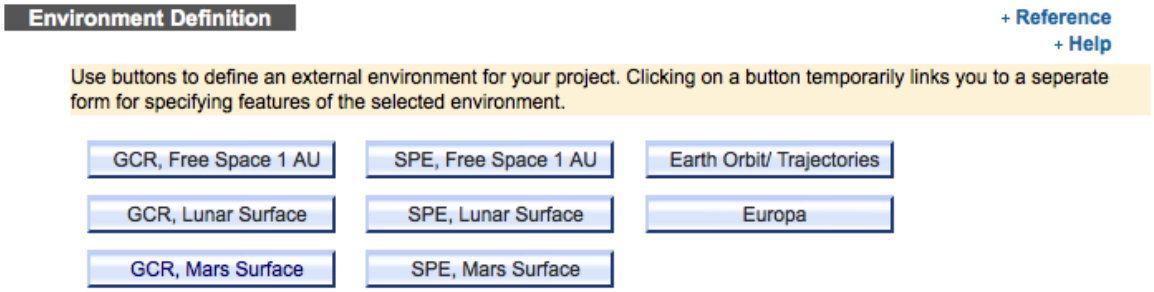

Figure 3.1. Environment Definitions in OLTARIS
(*Credit: OLTARIS*)

GCR Environments

This GCR environment is based on balloon- and satellite-measured energy spectra from 1954 to 1992 and measurements from the Advanced Composition Explorer (ACE) satellite from 1997 to 2002 that has fitted with the stationary Fokker-Planck equation.[3]

This fit solves the diffusion, convection, and energy loss boundary value problem, and obtains an estimate of an appropriate ``diffusion coefficient.'' These coefficients are seen to fluctuate on a 22-year period, correlating with the solar minima and maxima. For periods situated in between available data, the correlation of this diffusion coefficient with the Climax Neutron Monitor[4] data allows an estimation of the diffusion coefficient for these intermediary times.

[3] The Fokker–Planck equation is a partial differential equation that describes the time evolution of the probability density function of the velocity of a particle under the influence of drag forces and random forces, as in Brownian motion.

[4] An experiment out of Climax, Colorado that measures space neutron fluxes.

The end result of this environment's implementation is a single value of the deceleration parameter, which describes the level of solar cycle modulation and determines the GCR differential energy spectrum for elements from hydrogen to nickel at any given radial distance from the sun (OLTARIS) (Badhwar 1994). There are currently eleven preset scenarios available for user selections:

Scenario	Deceleration Parameter
1956 Solar Minimum	401
1959 Solar Maximum	1986
1965 Solar Minimum	510
1970 Solar Maximum	1293
1977 Solar Minimum	474
1982 Solar Maximum	1924
1987 Solar Minimum	467
1991 Solar Maximum	2525
1997 Solar Minimum	467
2000 Solar Maximum	1674
2007 Solar Minimum	490

Table 3.1. Deceleration Parameters for Preset OLTARIS GCR Scenarios

The output of the external environment module has units of either spectral flux or spectral fluence (flux/fluence, with respect to particle energy) – particles/(cm^2-time-AMeV) – depending on the environment chosen. For GCR and Earth Orbit (EO) environments, time is given in days and renders a flux output. This boundary condition defines the units used in the rest of the OLTARIS processes.

SPE Environments

The historical SPE events in OLTARIS are calculated using differential formulas. The output of the external environment module has units of either spectral flux or spectral fluence (flux/fluence, with respect to particle energy) – particles/(cm^2-time-AMeV) -- depending on the environment chosen. For SPE environments, time is measured in events, rendering a fluence output. This boundary condition defines the units used in the rest of the OLTARIS processes.

Once the particles' spectra have been defined on the external boundary of the spacecraft through the environment module, transport through bulk matter is initiated.

Other Environments

The **Earth Orbit (EO)** environment includes trapped protons, albedo neutrons and a modulated GCR environment. The EO trajectory can be circular, based on altitude, inclination and date, or user-uploaded. If the user inputs a custom trajectory, OLTARIS can compute responses averaged over the entire trajectory or at each point along the trajectory (Sandridge 3056).

Any **Lunar Surface** environment includes the neutron albedo for both interpolation-based and ray-by-ray transport (Sandridge 3056).

Any **Mars Surface** environment includes both atmospheric and albedo effects. The MARS-Gram 2001 model is used for the atmosphere, whose thickness varies with surface elevation and ray-direction with respect to the horizon. The Mars surface environments are run only for thickness distributions using ray-by-ray transport, where the appropriate amount of atmosphere and surface regolith are automatically added to the user-provided thickness distributions (Sandridge 3056).

The **Europa** environment is the design reference environment for the joint NASA/ESA unmanned mission ``EJSM/Laplace.'' The radiation environment consists of trapped electrons, omnidirectional trapped protons, and trapped heavy ions (OLTARIS).

Material Properties

OLTARIS supports aluminum, polyethylene, and tissue as default materials within a vehicle (OLTARIS). However, capabilities have been added in the last few years for the user to define their own material databases, define multi-layered slabs and spheres with any number of materials, and to upload ray-traced thickness distributions with any number of materials[5] (Sandridge 2008). Therefore, any number of configurations is theoretically available, and three-dimensional geometry can be *partially* recreated through careful choice of material distributions.[6] However, OLTARIS does not allow for ``empty space'' – there can be no empty vacuum for particles to be transported through, making 3-D geometry where there is space between materials a challenge to recreate in the 1-D code!

The **cross-sectional database module** determines how particles transport through a material. OLTARIS uses NUCFRG2 - ``a classical, geometric model based on the abrasion - ablation concept, whereby a piece of the incoming projectile nucleus is sheared off (abraded) by collision with the target'' (OLTARIS). The model is geometric in the sense that it treats the projectile and target nuclei as colliding spherical objects; it is classical in the sense that it neglects any quantum mechanical effects and includes no information about the shell structure of either nuclei. This produces many weaknesses and approximations in the code output, which cannot be easily approximated in a general manner.[7]

Geometry

The geometry of an OLTARIS input can be defined in three separate ways: via a slab definition, a sphere definition, or a thickness distribution.

---

[5] As will be mentioned, human phantoms like MAX and FAX take advantage of this feature.

[6] E.g., a 1cm Aluminum thickness atop a 20 cm air thickness is approximately equivalent in one dimension to a 1 cm aluminum ``sphere'' 20 cm from the center of an air-filled sphere!

[7] One weakness with NUCFRG2 is its inability to account for the so-called ``odd-even effect'' (OLTARIS) – cross sections for fragments with an even number of nucleons are consistently larger than those of fragments with an odd number of nucleons -- a phenomenon related to the nuclear pairing interaction, a quantum mechanical effect.

Slab Definition

The **slab** computation transports particles from the chosen boundary condition, through any user defined materials and thicknesses, and generates fluxes/fluences at material interfaces and at the end boundary/target (OLTARIS).

Sphere Definition

The **sphere** computation transports particles from the chosen boundary condition through a one-dimension section of a ``sphere'' of a specified material and thickness -- essentially, it places the sphere's material(s) atop any inside phantom or material, and transports particles through the outermost layer first. OLTARIS' geometry has been updated to include user-defined spherical shells; these can include any number of materials, with any thicknesses, and in any order.

If calculating effective dose as a response function, an orientation-averaged phantom is used in order to reduce asymmetric biases coming from the position of the phantom inside the sphere (Sandridge 3056).

Thickness Distribution

The computation for the case of a **thickness distribution** is a series of transport runs for an array of depths for each material that the user needs (OLTARIS). The purpose of this geometry is to provide a custom-shaped shielding distribution, and to help more accurately model shielding that cannot easily be broken down into one-dimensional arrays. This is the shielding that this research used, since the provided aluminum spheres in this section are some of the simplest geometries available to OLTARIS.

Transport

OLTARIS uses **HZETRN** (**HZE TR**a**N**sport) as the engine of its radiation transport code. HZETRN uses a straight-ahead (1-D) approximation along a ``ray'', the goal of which being the speed of the calculation afforded by such an approximation. For rays along which particles are propagated through three materials or less, the thickness distribution is calculated by computing ``flux vs. depth'' for varying thicknesses, creating an interpolation table to enable fast calculations along each ray, and afterwards integrating all responses along all rays to determine the total response for the system. This ignores certain scattering particles and other minor approximations, which are assumed to be minimal when so few materials are being used. Thickness distributions with more than three materials, however, use a ``ray-by-ray'' process, in which a full transport with bi-directional neutrons is performed for each ray in the distribution, rather than an interpolation table (Sandridge 3056). In the case of slab and spherical geometries, an addition of a coupled bi-directional neutron is included to increase the accuracy of the response, while not substantially decreasing its run-time.

Response Functions

The type of ``response'' (output) calculated by HZETRN is dependent wholly on the user's choice - OLTARIS does not compute any output not explicitly requested be the user on the web interface of the program. OLTARIS is currently focused on *human* responses to radiation (Sandridge 3056), and include dose, dose equivalent, effective dose equivalent, Linear Energy Transfer (LET), and TLD-100/TEPC instrument readings, which are currently used for validation of the OLTARIS code.

The response is calculated with the result of the transport module (a flux or fluence, depending on the environment chosen). For thickness distribution geometries, the total quantity of radiation at a target point is found by integrating over all rays, each of which has its own ``[response function] vs. depth'' curve calculated during transport.[8]

In the case of effective dose equivalent, the user can choose one of four body phantoms (see next section), which is then added to their thickness distribution when computing the response. The processing for calculating dose equivalent at a single target point is repeated for *each organ*, and a weighted average of these values is taken (the weights are decided by ICRP60 quality factors, defined in Table 2.4). For the whole body effective dose equivalent calculation, each weighted effective dose equivalent is summed according to ICRP60 guidelines.

After the response functions have been calculated, an E-mail alerts the user that the results are available for viewing in the user's account.

Human Phantoms in OLTARIS

If the user selects an effective dose equivalent response function, the user must also choose a human phantom supported by OLTARIS on which these calculations can be made. There are currently four available phantoms: CAM, CAF, MAX05, and FAX05.

CAM and CAF

The **CAM** (**C**omputerized **A**natomical **M**ale) and **CAF** (**C**omputerized **A**natomical **F**emale) models in OLTARIS are human phantoms created by Billing and Yucker in 1973 (Billing 1973). For this paper, CAM and CAF are to be omitted from any analysis for two reasons. First, they are lacking the ability to calculate organ equivalent doses for spongiosa bone, the retina (or any part of the eye), the small intestine, and the trachea. Second, MAX05 and FAX05 are more easily compared to the human phantoms found in MCNP6, for reasons described below.

[8] The selection of the thickness intervals in this curve is dependent on the boundary condition, and not user selectable as of March 2015.

MAX05 and FAX05

The MAX (Male Adult voXel) and FAX (Female Adult voXel) human phantoms were created by the CalDose team in Recife, Brazil in 2005. MAX and FAX have the ability to calculate dose equivalent for 27 organs. They also calculate whole body effective dose equivalent using the ICRP60 values, and the additional ``remainder organ'' values listed in Table 4 (OLTARIS).

Organ	Quality Factor - MAX	Quality Factor - FAX
Adrenals	0.05/9	0.05/10
BFOs	0.12	0.12
Bladder	0.05	0.05
Bone, Cortical	0.01	0.01
Bone, Spongiosa	N/A	N/A
Brain	0.5/9	0.05/10
Breasts	0.05	0.05
Colon	0.126	0.125
Heart	N/A	N/A
Hippocampus	N/A	N/A
Kidneys	0.5/9	0.5/10
Lens	N/A	N/A
Liver	0.05	0.05
Lungs	0.12	0.12
Muscle	0.05/9	0.05/10
Oesophagus	0.05	0.05
Ovaries	–	0.20
Pancreas	0.05/9	0.05/10
Prostate	N/A	–
Retina	N/A	N/A
Salivary Glands	N/A	N/A
Skin	0.01	0.01
Small Intestine	0.05/9	0.05/10
Spleen	0.05/9	0.05/10
Stomach	0.12	0.12
Testes	0.20	–
Uterus	–	0.05/10
Thymus	0.05/9	0.05/10
Thyroid	0.05	0.05
Trachea	N/A	N/A

Table 3.2. ICRP60 Quality Factors As Divided in MAX and FAX

For both MAX and FAX, the ``colon'' is the colon (quality factor 0.12) plus the large intestine (quality factor 0.05/9 and 0.05/10, respectively). The ``remainder'' quality factor from ICRP 60 is spread evenly across nine organs in MAX, and ten organs in FAX. And while the organ averaged dose equivalent is calculated for several organs (such as the lens of the eye, the heart, and the trachea), these organs are not used in the calculation of the whole body effective dose equivalent.

MCNP6 (Monte Carlo N-Particle, version 6) and its legacy codes are descended from the ENIAC machine, created by Metropolis and Ulm during the Manhattan Project (Metropolis 1949). The latest iteration of this code - MCNP6.1.1, released in 2011 (hereafter, simply ``MCNP6'') - is a combination of MCNP5 and MCNPX. MCNP6 marks the first production version of a Monte Carlo code that can perform complex calculations on a voxelized human phantom (see MASH & FASH, below) with the needed resolution (voxels are 1.2 cubic millimeters in size) *and* have the capacity to transport the required exotic particles found in deep space.

The Input Deck

The heart of MCNP6 is the input deck - the base text code written by the user that sets up the scenario and all relevant factors for calculation by MCNP6. There are effectively infinite input decks that can be created, and any interested parties should consult the MCNP User's Manual for a full listing of the capabilities of this program. This overview will only cover the cards and commands used in the creation of the OLTARIS-like scenarios run for this paper. The important input deck sections (called ``cards'') include the cell card; the surface card; and other data cards like the physics card, particles card, materials card, source card, and any tally cards.

Cells, Surfaces, and Universes

Perhaps the most important and complex aspect of MCNP6 is the defining the geometry of the problem to be studied by the user. MCNP6 accomplishes this through the use of **cells**, **surfaces**, and **universes**.

Cells

Cells are three-dimensional volumes of essentially any size, bounded by surfaces specified in the card after this. The cell card must be the first entry on the input deck after the required problem title card, and each distinct cell must be defined here (MCNP Manual, p.23). Each unique cell is assigned a unique *cell number* (e.g., "9999"), and usually a *cell material number* matching a material number on the Materials card – both numbers not exceeding eight digits in length. Next is the *cell material density number*; a positive number here is interpreted as an atomic density (units of 10^{24} atoms/cm^3), while a negative entry is interpreted as a mass density (units of grams/cm^3). Following these two identifiers and density specification, a collection of cells with materials have been created with no specific location; the geometry of the cell is then needing to be defined, to place these cells in the proper configuration.

Surfaces

Surfaces are two-dimensional mathematical entities, used to define the edges of cells and the origin of radiation sources (MCNP Manual p.23). The most common surfaces used are planes and spheres.

To define these surfaces, the first entry on the surface card is the *surface number*, for identification purposes (similar to the cell number, it must not exceed eight digits). The second entry is an alphabetic *surface mnemonic* indicating the surface type (e.g., a YZ plane). Following the surface mnemonic are the *numerical coefficients* of the equation of the surface, in the order listed below:

Surface Mnemonic	Surface Equation	Coefficients
PX	$x - D = 0$	D
PY	$y - D = 0$	D
PZ	$z - D = 0$	D
S	$(x - \bar{x})^2 + (y - \bar{y})^2 + (z - \bar{z})^2 - R^2 = 0$	$\bar{x}$, $\bar{y}$, $\bar{z}$, R

So for the planes (PX, PY, and PZ), D is the value of the point where the plane crosses the specified axis (e.g., ``1 PX -3'' would be a plane, with surface number 1, located at x = -3). Some clever manipulation could defined a cube, say, of side length 6, using six surfaces, like so:

1	PX	-3
2	PX	3
3	PY	-3
4	PY	3
5	PZ	-3
6	PZ	3

This method was used to create a **voxel** – a three-dimensional bit that is essential for incorporating a voxelized human phantom like MASH or FASH.

Universes

To create an environment capable of holding a voxelized human phantom like MASH or FASH, a relatively new feature of the MCNP code -- lattices and universes -- was utilized in the input deck. **Universes** can be thought of as a lattice of cells, or a large cell subdivided into many cells (MCNP Manual p.87). The advantage of a universe over multiple cells is the ability to manipulate a number of distinct cells all at once, rather than individually.

The Human Phantoms - MASH & FASH

MASH (the **M**ale **A**dult me**SH** phantom) and **FASH** (the **F**emale Adult me**SH** phantom) are two human phantoms – computerized computational models of a male and female body - created by the CALDose team of Department of Nuclear Energy at the Federal University of Pernambuco in Recife, Brazil (Kramer 2010). MASH and FASH are the result of years of work improving on the previous CALDose phantoms MAX and FAX, which are two of the phantoms currently supported by OLTARIS. They were developed using 3D animation software to replace the image-based FAX06 and the MAX06 voxel phantoms.

In the case of integrating MASH and FASH into the MCNP6 architecture, treating each phantom as a universe within MCNP6 allows one to move the phantom within the space of MCNP6 all together, rather than voxel by voxel. This makes orienting the phantom within the MCNP6 geometry much simpler, and allows for quick referencing of the phantom rather than

individual cells and materials. In total, 122 cells were defined in MASH, each with its own material ID and density (see Appendix A). Together with the materials defined in the following sections, an entire ICRP-110 compliant human voxel phantom was successfully encoded into MCNP6.

Surrounding the phantom, an aluminum spherical surface was placed 500 cm away from the center of mass of the phantom, and given a thickness of either 20 g/cm^2 or 0.4 g/cm^2, depending on the replicated OLTARIS scenario. Outside of this sphere, a second ``source sphere'' was placed at 510 cm, from which the transported source particles (GCR or SPE) would flow.

The CEM and LAQGSM Event Generators

Handing all ion interactions are the **C**ascade-**E**xciton **M**odel (**CEM**) and the **L**os **A**lamos **Q**uark **G**luon **S**tring **M**odel (**LAQGSM**).

CEM

For these simulations, CEM is used to transport light particles like the carbon nuclei and below of low-to-intermediate energies (less than 1 GeV). It calculates nuclear reactions induced by neutrons, protons, pions, and photons (Mashnik 2008). It recreates these reactions in four steps:

- The Intranuclear Cascade (INC) Mechanism Stage
- The Coaslescence Model Stage
- The Pre-Equilibrium Stage (or Fermi Breakup Model Stage)
- The Equilibrium Evaporation/Fission Stage

The **INC Mechanism Stage** assumes that intra-nuclear cascades caused by source particles ``are a series of successive quasi-free collisions of the fast primary particle with the individual nucleons of the nucleus'' (Mashnik 2008). It is a calculation carried out in three dimensions, where the target nucleus is divided into seven zones of concentric spherical shells; over each zone, the nuclear density is assumed to be constant. The energy of the target nucleus is determined with the perfect Fermi-gas approximation; the nucleus's effective real potential is added to the kinetic energy of the projectile when considering the total energy of the system (because of the effect on the collisions by nearby nucleons); and the Pauli exclusion principle is also taken into account. This last influence excludes a number of possible collisions, ``effectively increas[ing] the mean free path of the cascade particles inside the target [object].'' The nuclear cross sections of all of these collisions are approximated through an extrapolation of experimental data, available since 2008 (Mashnik 2008).

The **Coalescence Model Stage** begins once the cascade stage has completed. In this stage, high-energy deuterium, tritium, ^{3}He and alpha particles are created around the cascade particles, with momenta determined via parameters influenced by their mass and the cascade particle's initial momentum. If the mass number is greater than 13, the code moves onto the Pre-Equilibrium Stage; if the mass number is less than 13, the Fermi breakup model (produced by Dr. Barashnikov in Dubna, Russia) is used.

In the **Pre-Equilibrium Stage**, all possible nuclear transitions are taken into account, as well as all possible multiple subsequent emissions of neutrons, proton, deuterium, tritium, ^{3}He and alpha particles. These transitions and their probabilities are then taken into account and solved via the Monte Carlo method.

In the **Equilibrium Evaporation/Fission Stage**, the code calculates the probability of the evaporation of nucleons, complex particles and light fragments heavier than ^{4}He, up to ^{28}Mg, in the target nucleus (Mashnik 2008) (*evaporation* meaning, in this case, the extreme excitation of the target nucleus and the subsequent separation of nuclear particles from the atom (Lopez 2000)). If a charged particle is selected for evaporation, it does so; if a neutron is selected for evaporation, the probability of fission is calculated and the program chooses either evaporation or fission based on this probability. If fission is chosen, the mass, charge, and energy distribution of fission fragments is simulated using extrapolations of available experimental data. Users can choose to transport all 66 nucleons in this stage, or, to save computing time, only the lightest six mentioned in the pre-equilibrium stage. Either way, all remaining particles are transported to their chain's ultimate end, and the process begins again for the next source particle.

LAQGSM

The basic mechanics of LAQGSM are very similar to the mechanisms described above for CEM. The major difference in the two event generators is the energy level at which the particles are created. CEM describes interactions of particles below about 1 GeV; however, it does not take into account something called the ``trawling effect,'' in which ultra high-energy particles in a cascade will deplete the target nucleons in the system (Mashnik 2008). For these high energies where the effect is significant, LAQGSM is better than CEM for approximating the reactions taking place on the subatomic scale.

Validation of CEM and LAQGSM

Due to the integral nature of this part of MCNP6, CEM and LAQGSM should be expected to have a high level of validation and verification; and indeed, this is so. These event generators have been compared to experimental data ranging from ~10 MeV per nucleon, up to ~1 TeV per nucleon (orders of magnitude above the highest expected energy of a GCR particle) (Mashnik 2008). Therefore, it is safe to assume that for most particle energies involved in this simulation, CEM and LAQGSM are more than accurate enough to provide valid estimates of space radiation dose.

Particles Transported In MCNP6

Because of the combination of MCNPX with MCNP5, MCNP6 is now able to transport a number of exotic particles found only in high-energy accelerators and space radiation environments. The full list of particles transported by MCNP6, with their MCNP6 particle symbols bracketed, are in Table 2.5.

Baryons		Mesons		Leptons		Gauge Bosons	
n	[n]	Π^+	[/]	e^-	[e]	γ	[p]
p	[h]	Π^0	[z]	e^+	[f]		
Λ^0	[l]	Π^-	[*]	μ^-	[|]		
Σ^+	[+]	K+	[k]	μ^+	[!]		
Σ^-	[-]	K-	[?]	ν_e	[u]		
Ξ^0	[x]	K_L^0	[^]	ν_m	[v]		
Ξ^-	[y]	K_S^0	[%]	$\bar{\nu}_e$	[<]		
Ω^-	[o]			$\bar{\nu}_e$	[>]		
$\bar{n}$	[q]						
$\bar{p}$	[g]						
$\bar{\Lambda}^0$	[b]						
$\bar{\Sigma}^+$	[-]						
$\bar{\Sigma}^-$	[ ]						
$\bar{\Xi}^+$	[w]						
$\bar{\Xi}^0$	[c]						
$\bar{\Omega}^-$	[@]						
d	[d]						
t	[t]						
^{3}He	[s]						
α	[a]						
$3 > Z > 100$	[#]						

Table 3.3. Particles Transported By MCNP6

Since OLTARIS only transports neutrons, protons, deuterons, tritons, helions, alpha particles, and some heavy ions (3>Z>100), the OLTARIS scenarios recreated in MCNP6 only transport those same particles.

The Materials Card

The materials card has the format

[Mm] [ZAID1] [fraction1] [ZAID2] [fraction2]...

Where *m* is a material ID number less than five digits, *ZAID* is the nuclide identification number, and *fraction* is the fraction of the material that is the nuclide previously identified.

The **nuclide identification number** has, omitting extraneous tags, the form ZZZAAA. ZZZ is the element or nuclide's atomic number, and AAA is the element or nuclide's mass number (Goorley 2012). For naturally occurring elements, AAA=000. The **nuclide fraction** can be stated in two ways: as a weight fraction or as an atomic fraction. If the fraction is entered with a negative number, it is a weight fraction; if it is entered as a positive number, it is an atomic fraction.

For this run, a total of 86 materials were defined (see Appendix A for the full list). The majority of these were created from the definitions and mass densities provided in ICRP 110; because of this, the MASH and FASH models created in these scenarios are ICRP 110-compliant.

The Source Card

The source card provides MCNP6 with directions for where to run the particles from, and in what manner. Every MCNP6 problem has one of four sources: general source (SDEF), surface source (SSR), criticality source (KCODE), or a user-supplied source. To recreate the scenario in OLTARIS as close as possible, two sources were supplied to be run in separate trials: to model galactic cosmic rays, GCR77; and the same LaRC SPE spectrum used in OLTARIS was used in MCNP6.

Each source was defined to be isotropic. It was set at 510 cm away from the human phantom's center of mass, on surface #20, and directed inwards towards the phantom (by giving all particles leaving surface #20 away from the phantom an importance of 0 - essentially stopping the transport).

Tally Cards

The tally cards are important for what they can supply the user with -- information about the run itself. With no tallies (counts), there are no results displayed to the user; each run, the user must specify what quantifiable, countable values are important.

A number of tallies were created for each phantom. It was decided that both dose and dose equivalent tallies were to be created for each run, for each of the organs in the phantoms. For both MASH and FASH, this resulted in 54 tallies each.

In converting from dose to dose equivalent, MCNP6 uses NASA's own Q-values, which are identical to those used in OLTARIS. Also of note, the output of the dose equivalent tally is created in units of sieverts per hour; each result was multiplied by 0.277777777778 to convert to units of mSv/day, units used by OLTARIS.

Miscellaneous Cards

Of the remaining cards, the most important is the number of particles chosen to run, which directly affects the statistical certainty of the tallies' results. For each OLTARIS case, it was decided in the interests of time and feasibility that 14,000,000,000 source particles should be run -- 500,000,000 for every source isotope. If the results are inconclusive, merely allotting more time per run and increasing the number of particles will increase the statistical robustness of the comparison (assuming that the geometry and other assumptions are valid).

Chosen OLTARIS Projects for Replication

It was decided that the simplest geometry possible within OLTARIS - an aluminum ``sphere'' surrounding the human phantom - would be best suited to be modeled by MCNP6 for these first trials. The reasoning is straightforward - the implementation of MASH and FASH into MCNP6 was the first of its kind to be attempted, so there were likely to be many sources of error along the way. Beginning with an uncomplicated geometry, like a spherical shell, simplifies the creation of the MCNP6 input deck, while still providing meaningful error analyses for OLTARIS. Future research will be able model other schematics producible within OLTARIS and provide similar error analysis, once the human phantoms have already been consistently implemented.

For sources, two were chosen: GCR77, an ``average'' galactic cosmic ray source well analyzed by NASA and a commonly agreed upon ``default'' GCR source; and the LaRC SPE spectrum, which is similar to the one run on OLTARIS. Analyzing both of these situations, with simple geometry, should give the range of experience in deep space that are important to any mission: the long-term damage of GCRs, and the short-term life threatening dangers of SPEs.

For shielding thickness, two were chosen: aluminum spherical shield of 20 g/cm^2 and 0.4 g/cm^2. These thicknesses were chosen because they are the (approximate) thicknesses of spacecraft walls, and of astronaut spacesuits. Determining the effect of both sources on this simple geometric thickness will help scientists determine the extent of protection needed for long-range trips to Mars and beyond.

In total, eight scenarios were recreated in MCNP6 from OLTARIS:

Phantom	Al Shielding	Source
MASH	0.4 g/cm^2 (Suit)	GCR77
MASH	0.4 g/cm^2 (Suit)	LaRC SPE
MASH	20 g/cm^2 (Ship)	GCR77
MASH	20 g/cm^2 (Ship)	LaRC SPE
FASH	0.4 g/cm^2 (Suit)	GCR77
FASH	0.4 g/cm^2 (Suit)	LaRC SPE
FASH	20 g/cm^2 (Ship)	GCR77
FASH	20 g/cm^2 (Ship)	LaRC SPE

Challenges Mimicking OLTARIS in MCNP6

Different Physics: NUCFRG2 vs. CEM-LAQGSM

Perhaps the most insurmountable difference between OLTARIS and MCNP6 is their varied use of event generators and transport criteria. NUCFRG2 is a deterministic transport code; CEM-LAQGSM, on the other hand, is probabilistic in nature, and uses many more complicated steps and approximations to arrive at its output. There are no plans as of March 2015 to upgrade OLTARIS to be compatible with CEM-LAQGSM, and no plans to make MCNP6 compatible with a deterministic transport code. Such a pairing would not only be likely impossible, but highly

impractical and without much merit; one of the strengths of OLTARIS is its computational speed, which it accomplishes through estimating nuclear interactions through approximations like NUCFRG2. Any difference in output between these two codes must acknowledge to come from, at least in part, this separation of basic physical process analyses.

Different Phantoms: MAX vs. MASH, FAX vs. FASH

MASH and FASH are vast improvements over MAX and FAX. One of the most noticeable differences is the the number of and resolution of the phantoms. With each voxel only 0.001728 cm^3 in size, MASH contains almost 42 million voxels; the smaller FASH contains just under 35 millions voxels.

As of March 2015, OLTARIS has yet to be upgraded to be compatible with MASH and FASH; however, this is an attainable goal should NASA decide to pursue it. Until then, the difference in phantoms, albeit two phantom generations created by the same researcher, is an inseparable part of the uncertainty in the comparison of these two codes.

Difference Dimensions: 3 Dimensions vs. 1 Dimension

Another fundamental, unchanging difference between OLTARIS and MCNP6: MCNP6 models particle interactions in a three-dimensional world. OLTARIS analyzes particle interactions, and makes reasonable approximations regarding its deterministic effects; however, it only analyzes individual particles along a single one-dimensional ray. This makes MCNP6 and OLTARIS fundamentally different; it is not merely a ``bug'' that can be fixed later. Acknowledging this, however, allows the remaining analysis to go on as unencumbered as possible.

Because OLTARIS is a one-dimensional code, and the use of the term ``sphere'' to describe the chosen shielding is misleading. What OLTARIS actually does is create a material thickness along the path of each ray -- e.g., a 20.0 g/cm^2 aluminum sphere surrounding a human body would place approximately 7.40 cm of aluminum *immediately in front of* the human tissue along the ray's path. OLTARIS then calculates the depth of the particle's path along the ray, using the slowing-down approximation and others. Because the best description of shielding with the same thickness from any direction towards the target is a ``sphere,'' this is the scenario modeled in MCNP6.

Ultimately, some error will always be a part of this imperfect combination of two radiation transport codes; however, the expected error difference is quantifiable and knowable (in theory), and therefore the analysis of the recreated OLTARIS code will yield valid insights into the one-dimensional transport engine. The following section lays out the results of the study, and compares the dose equivalent of each organ in MCNP6's eight runs to their OLTARIS counterpart.

CHAPTER 4

RESULTS

Male, Suit, GCR

Daily Organ Dose EQ/WBEDE [mSv]: Male, 0.4 g/cm^2 Al Sphere, GCR77				
	MCNP6		OLTARIS	% Difference
Organ	MASH		MAX05	
Adrenals	1.612	± 0.158	0.974	-39.60
BFO	2.438	± 0.052	1.125	-53.83
Bladder	1.998	± 0.238	1.027	-48.58
Cortical Bone	2.568	± 0.025		-52.24
Spongiosa Bone	2.231	± 0.023		-45.01
Bone (Total)			1.227	
Brain	2.532	± 0.052	1.339	-47.11
Breasts	2.278	± 0.113	1.229	-46.02
Colon	1.902	± 0.066	1.082	-43.09
Heart	1.906	± 0.082	1.146	-39.87
Hippocampus			1.281	
Kidneys	1.755	± 0.077	1.036	-40.97
Lens	2.518	± 0.400	1.624	-35.52
Liver	1.834	± 0.038	1.069	-41.72
Lungs	1.380	± 0.025	1.225	-11.23
Muscle	2.347	± 0.011	1.303	-44.49
Oesophagus	1.758	± 0.090	1.103	-37.27
Pancreas	1.878	± 0.163	0.975	-48.07
Prostate	1.526	± 0.165	1.004	-34.21
Retina	2.834	± 0.343	1.425	-49.71
Salivary Glands	2.637	± 0.164	1.421	-46.12
Skin	3.200	± 0.022	1.761	-44.98
Small Intestine	1.716	± 0.049	1.065	-37.94
Spleen	1.875	± 0.113	1.096	-41.54
Stomach	1.821	± 0.094	1.085	-40.43
Testes	2.207	± 0.108	1.371	-37.89
Thymus	1.926	± 0.131	1.147	-40.46
Thyroid	2.419	± 0.322	1.203	-50.26
Trachea	1.664	± 0.104	1.216	-26.90
WBEDE		±	1.183	-41.94

Table 4.1. Daily Organ Dose EQ/WBEDE [mSv]: Male, 0.4 g/cm^2 Al Sphere, GCR77

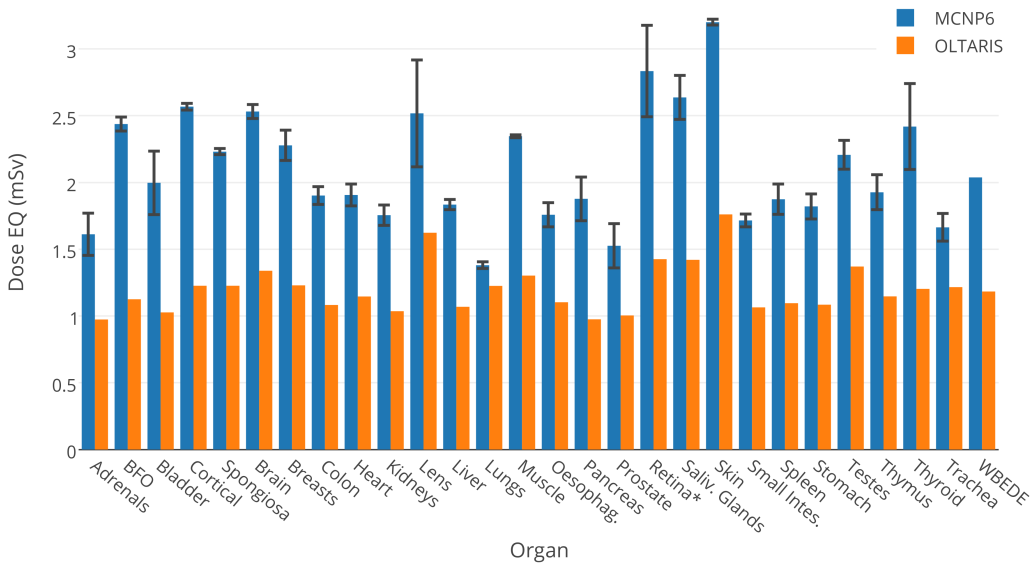

Figure 4.1. Organ and whole body equivalent doses for male phantoms with 0.4 g/cm^2 Al shielding in a GCR77 environment

Male, Ship, GCR

Daily Organ Dose EQ/WBEDE [mSv]: Male, 20.0 g/cm^2 Al Sphere, GCR77				
	MCNP6		OLTARIS	% Difference
Organ	MASH		MAX05	
Adrenals	1.308	± 0.199	0.781	-40.33
BFO	2.024	± 0.052	0.832	-58.87
Bladder	1.563	± 0.151	0.798	-48.94
Cortical Bone	2.010	± 0.024	–	-56.88
Spongiosa Bone	1.869	± 0.023	–	-3.63
Bone (Total)	–	–	0.867	–
Brain	2.100	± 0.051	0.910	-56.65
Breast	2.362	± 0.339	0.870	-63.18
Colon	1.639	± 0.070	0.818	-50.13
Heart	1.570	± 0.061	0.843	-46.34
Hippocampus	–	–	0.892	–
Kidneys	1.588	± 0.087	0.802	-49.49
Lens	1.632	± 0.278	0.992	-39.24
Liver	1.547	± 0.034	0.814	-47.38
Lungs	1.253	± 0.024	0.871	-30.53
Muscle	1.904	± 0.010	0.892	-53.14
Esophagus	1.778	± 0.329	0.828	-53.42
Pancreas	1.253	± 0.062	0.781	-37.67
Prostate	1.750	± 0.433	0.791	-54.82
Retina	1.646	± 0.123	0.935	-43.20
Salivary Glands	2.077	± 0.165	0.928	-55.31
Skin	2.437	± 0.021	1.039	-57.36
Small Intestine	1.554	± 0.057	0.812	-47.77
Spleen	1.512	± 0.085	0.823	-45.57
Stomach	1.413	± 0.075	0.820	-41.98
Testes	1.736	± 0.112	0.908	-47.70
Thymus	2.198	± 0.316	0.844	-61.59
Thyroid	2.007	± 0.230	0.860	-57.16
Trachea	1.317	± 0.093	0.866	-34.25
WBEDE	1.716		0.851	-50.39

Table 4.2. Daily Organ Dose EQ/WBEDE [mSv]: Male, 20.0 g/cm^2 Al Sphere, GCR77

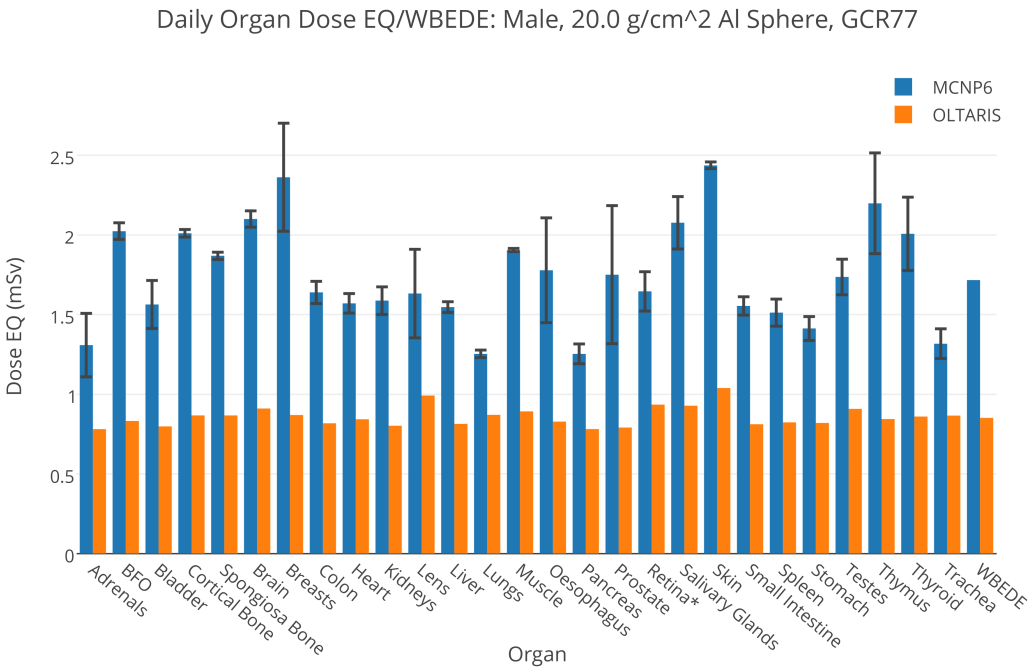

Figure 4.2. Organ and whole body equivalent doses for male phantoms with 20.0 g/cm^2 Al shielding in a GCR77 environment

Male, Suit, SPE

Event Organ Dose EQ/WBEDE [mSv]: Male, 0.4 g/cm^2 Al Sphere, LaRC August 1972 SPE				
	MCNP6		OLTARIS	% Difference
Organ	MASH		MAX05	
Adrenals	628.1	± 20.92	325.1	-48.24
BFO	4429	± 18.16	1558	-64.81
Bladder	783.9	± 14.82	648.1	-17.33
Cortical Bone	7618	± 11.43	–	-65.96
Spongiosa Bone	3989	± 7.18	–	-35.01
Bone (Total)	–	–	2593	–
Brain	4826	± 14.96	2071	-57.08
Breasts	1832	± 263.78	2000	-89.08
Colon	1937	± 13.17	910.5	-52.99
Heart	1149	± 8.85	1044	-9.14
Hippocampus	–	–	1524	–
Kidneys	1002	± 9.32	610.6	-39.04
Lens	1985	± 1030.12	17090	-13.90
Liver	1860	± 7.44	774.2	-58.38
Lungs	1694	± 5.08	1504	-11.23
Muscle	6318	± 3.79	2880	-54.41
Oesophagus	1041	± 19.68	760.3	-26.98
Pancreas	714.5	± 9.50	331.0	-53.68
Prostate	1382	± 51.56	457.9	-66.87
Retina	11310	± 224.98	4011	-64.53
Salivary Glands	13150	± 102.56	8051	-38.77
Skin	45080	± 27.05	44780	-0.66
Small Intestine	1008	± 6.05	766.8	-23.94
Spleen	1958	± 23.69	901.4	-53.96
Stomach	1588	± 16.99	848.1	-46.58
Testes	10230	± 148.29	5664	-44.62
Thymus	1823	± 39.38	889.9	-51.19
Thyroid	5245	± 119.59	1820	-65.30
Trachea	2158	± 66.48	1681	-22.08
WBEDE	5244.60		2538.97	-51.59

Table 4.3. Daily Organ Dose EQ/WBEDE [mSv]: Male, 0.4 g/cm^2 Al Sphere, SPE Environment

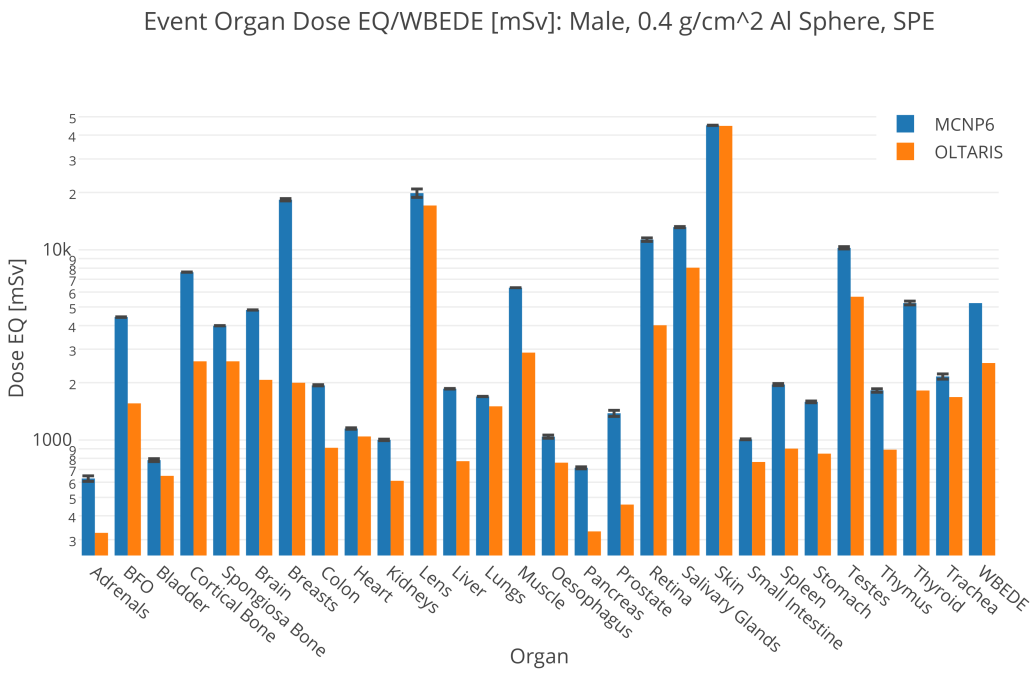

Figure 4.3. Organ equivalent doses for male phantoms within a LaRC August 1972 SPE environment (0.4 g/cm^2 Al shielding)

Male, Ship, SPE

Event Organ Dose EQ/WBEDE [mSv]: Male, 20.0 g/cm^2 Al Sphere, LaRC August 1972 SPE				
	MCNP6		OLTARIS	% Difference
Organ	MASH		MAX05	
Adrenals	85.73	± 7.60	68.53	-20.07
BFO	216.7	± 2.64	101.35	-53.23
Bladder	77.93	± 3.58	80.48	+3.27
Cortical Bone	200.1	± 0.82	–	-38.39
Spongiosa Bone	175.1	± 0.86	–	-29.59
Bone (Total)	–	–	123.29	–
Brain	221.8	± 1.64	141.54	-36.17
Breasts	348.5	± 13.73	123.01	-64.71
Colon	118.8	± 2.09	91.54	-22.92
Heart	109.2	± 2.80	102.63	-6.04
Hippocampus	–	–	127.75	–
Kidneys	95.11	± 2.77	81.69	-14.11
Lens	266.1	± 33.18	229.67	-13.69
Liver	118.3	± 1.25	88.15	-25.49
Lungs	114.3	± 0.93	118.94	+4.10
Muscle	208.1	± 0.35	140.21	-32.62
Oesophagus	98.84	± 6.47	92.89	-6.02
Pancreas	85.07	± 5.33	68.86	-19.06
Prostate	97.04	± 7.56	74.78	-22.94
Retina	264.3	± 11.39	167.37	-36.68
Salivary Glands	268.6	± 5.32	174.81	-34.92
Skin	410.4	± 1.15	279.10	-32.00
Small Intestine	91.69	± 1.59	87.59	-4.47
Spleen	123.2	± 3.65	93.32	-24.22
Stomach	114.9	± 4.97	91.30	-20.52
Testes	244.7	± 7.58	165.13	-32.51
Thymus	131.7	± 9.27	100.70	-23.54
Thyroid	202.0	± 9.27	117.45	-41.84
Trachea	135.1	± 10.65	118.57	-12.25
WBEDE	173.270		115.38	-33.41

Table 4.4. Daily Organ Dose EQ/WBEDE [mSv]: Male, 20.0 g/cm^2 Al Sphere, SPE Environment

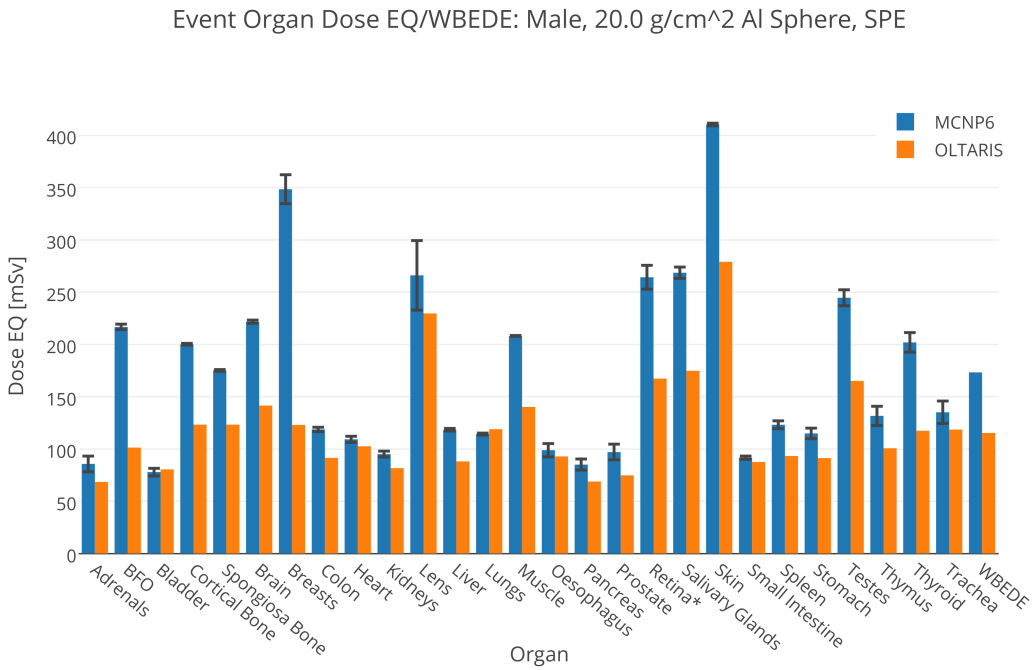

Figure 4.4. Organ equivalent doses for male phantoms within a LaRC August 1972 SPE environment (20.0 g/cm^2 Al shielding)

Female, Suit, SPE

Event Organ Dose EQ/WBEDE [mSv]: Female, 0.4 g/cm^2 Al Sphere, LaRC August 1972 SPE				
	MCNP6		OLTARIS	% Difference
Organ	FASH		FAX05	
Adrenals	1259	± 41.03	515.08	-59.07
BFO	4981	± 23.41	2147.68	-56.88
Bladder	1146	± 24.63	675.49	-41.03
Cortical Bone	7838	± 12.54	–	-57.79
Spongiosa Bone	4252	± 8.50	–	-22.18
Bone (Total)	–	–	3308.75	–
Brain	4947	± 15.83	2426.02	-50.96
Breasts	19240	± 73.10	5787.50	-69.91
Colon	1955	± 13.10	1310.14	-32.97
Heart	1694	± 13.55	800.43	-52.74
Hippocampus	–	–	1699.28	–
Kidneys	2217	± 19.29	776.73	-64.97
Lens	21290	± 1303.21	14667.49	-31.12
Liver	2202	± 9.25	1125.14	-48.89
Lungs	2931	± 8.50	2651.21	-9.53
Muscle	5567	± 4.45	2969.65	-46.66
Oesophagus	1873	± 34.84	923.55	-50.69
Pancreas	928.8	± 12.17	499.30	-46.24
Uterus	760.8	± 13.31	435.80	-42.72
Retina	13380	± 247.53	4717.73	-64.74
Salivary Glands	11230	± 101.07	8144.63	-27.48
Skin	46430	± 32.50	44533.13	-4.10
Small Intestine	1121	± 6.73	965.02	-13.90
Spleen	3102	± 35.05	1136.87	-63.35
Stomach	1815	± 19.06	932.01	-48.65
Ovaries	760.6	± 28.29	533.90	-29.80
Thymus	2832	± 61.16	2290.20	-19.12
Thyroid	10610	± 201.58	3684.02	-65.28
Trachea	4188	± 141.55	2192.76	-47.64
WBEDE	4015.8758		2106.53	-47.54

Table 4.5. Daily Organ Dose EQ/WBEDE [mSv]: Female, 0.4 g/cm^2 Al Sphere, SPE Environment

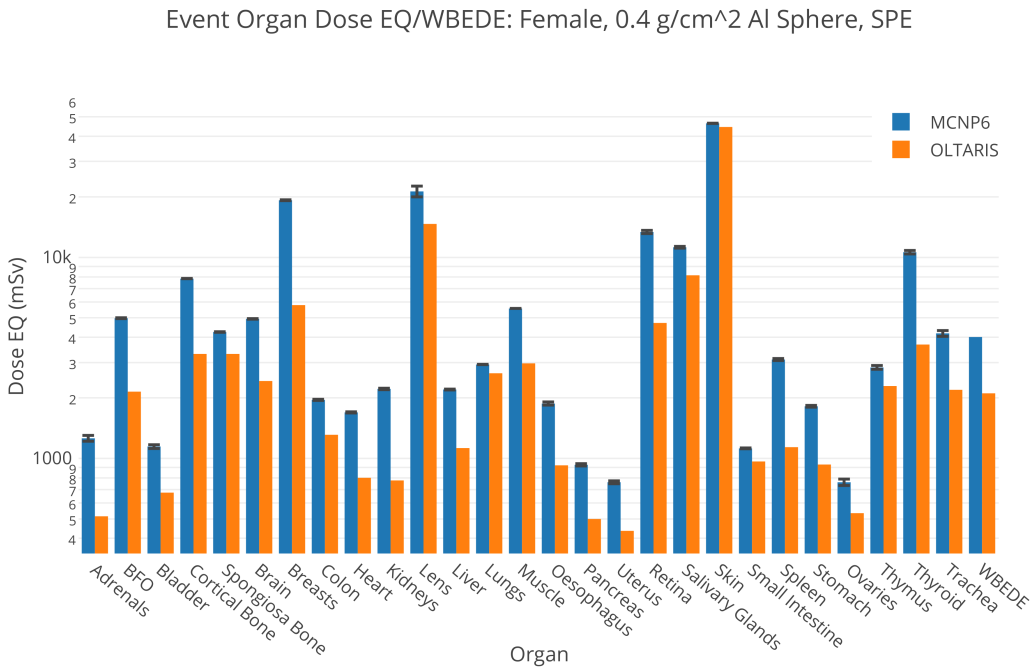

Figure 4.5. Organ equivalent doses for female phantoms within a LaRC August 1972 SPE environment, (0.4 g/cm^2 Al shielding)

Female, Ship, SPE

Event Organ Dose EQ/WBEDE [mSv]: Female, 20.0 g/cm^2 Al Sphere, LaRC August 1972 SPE				
	MCNP6		OLTARIS	% Difference
Organ	FASH		FAX05	
Adrenals	101.3	± 9.40	79.60	-21.46
BFO	227.1	± 3.41	114.68	-49.50
Bladder	89.39	± 4.13	83.42	-6.67
Cortical Bone	209.9	± 1.01	–	-34.97
Spongiosa Bone	184.7	± 0.98	–	-26.12
Bone (Total)	–	–	136.47	–
Brain	226.5	± 1.72	151.21	-33.23
Breasts	344.8	± 3.52	183.64	-46.75
Colon	127.1	± 2.45	103.50	-18.59
Heart	124.5	± 2.78	95.30	-23.44
Hippocampus	–	–	134.81	–
Kidneys	133.2	± 3.00	90.63	-31.94
Lens	246.8	± 33.94	239.38	-3.01
Liver	133.34	± 1.45	101.25	-24.09
Lungs	149.4	± 1.08	147.72	-1.16
Muscle	199.8	± 0.44	143.58	-28.15
Oesophagus	133.3	± 5.69	100.94	-24.26
Pancreas	96.79	± 5.37	79.64	-17.71
Uterus	82.31	± 5.17	75.71	-8.02
Retina	272.9	± 11.54	176.26	-35.42
Salivary Glands	293.5	± 7.16	181.91	-38.03
Skin	411.6	± 1.36	278.60	-32.31
Small Intestine	96.14	± 1.60	94.74	-1.46
Spleen	160.73	± 4.68	104.04	-35.27
Stomach	121.9	± 3.83	97.08	-20.33
Ovaries	67.99	± 5.21	80.08	+17.79
Thymus	153.6	± 8.23	136.73	-10.99
Thyroid	247.2	± 11.12	151.96	-38.52
Trachea	210.2	± 30.25	132.54	-36.96
WBEDE	151.01		112.08	-25.78

Table 4.6. Daily Organ Dose EQ/WBEDE [mSv]: Female, 20.0 g/cm^2 Al Sphere, SPE Environment

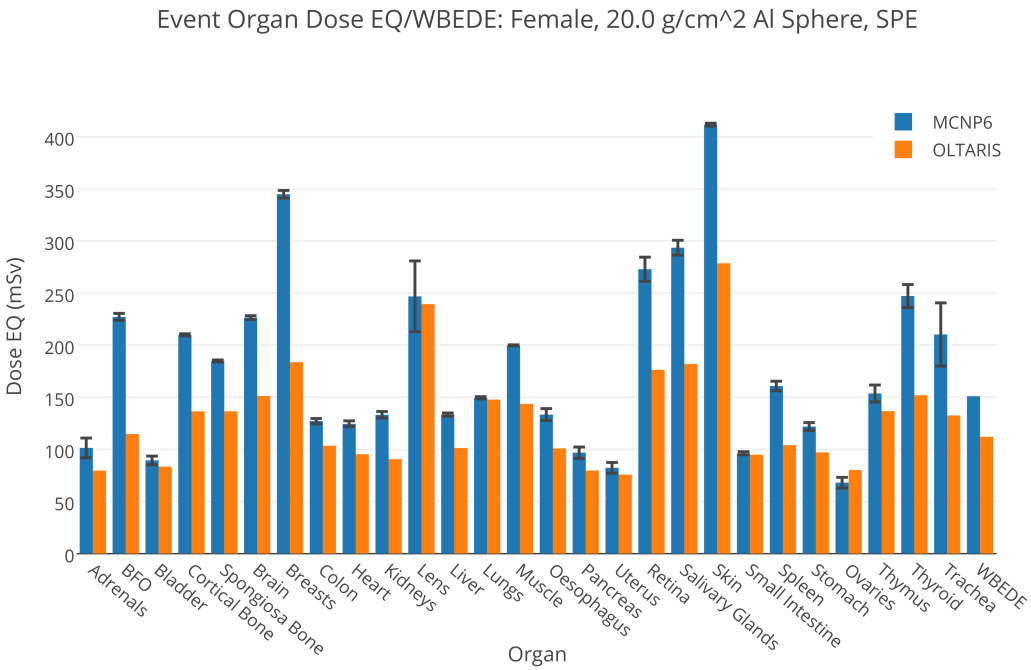

Figure 4.6. Organ equivalent doses for female phantoms within a LaRC August 1972 SPE environment, (20.0 g/cm^2 Al shielding)

CHAPTER 5

DISCUSSION

Some irregularities in the data must be addressed before it is interpreted:

- The Cortical Bone and Spongiosa Bone cells in MCNP6 were compared with OLTARIS dose over the entire bone structure.
- The retina dose calculated in OLTARIS was compared to the entire eye in MCNP6 - the size of the retina versus the eye is close enough to unity that, although there will be theoretical discrepancies in their calculated dose equivalent, the difference is not likely to be the most significant contribution to error.
- With the same reasoning, the hippocampus calculation from OLTARIS was excluded from comparison with the brain in MCNP6: no hippocampus cells were explicitly defined in MASH or FASH, and the volume the brain greatly exceeds the hippocampus alone, significantly skewing the comparison.

Overview

A common trait among all six scenarios sampled by MCNP6 is the **consistent underestimation of organ dose equivalent and whole body effective dose equivalent by OLTARIS**. Looking at Figure 5.1, the majority of organs had between 30% and 60% errors (treating MCNP6 as the validation data).

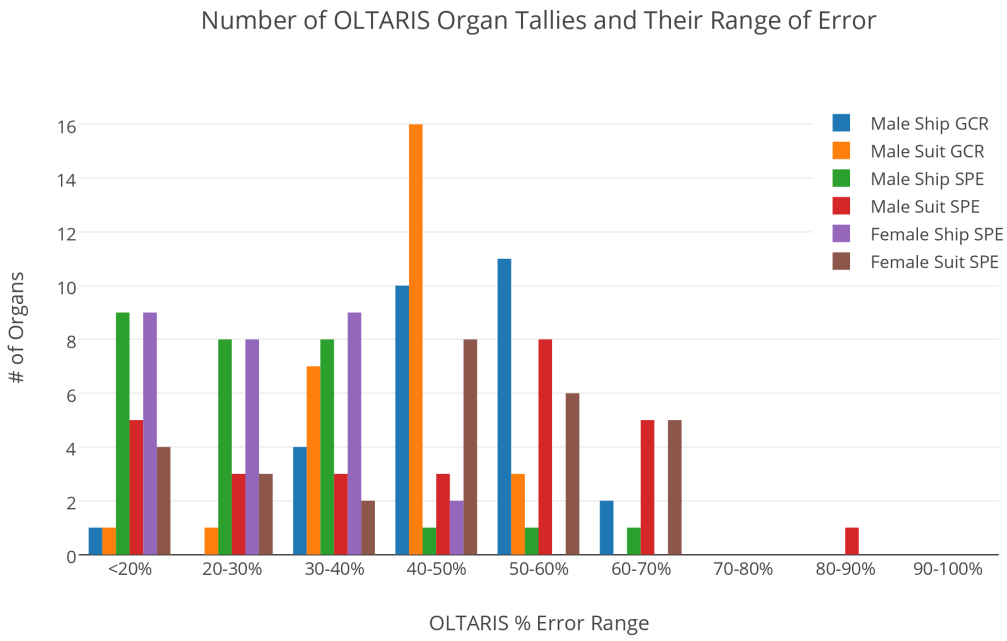

Figure 5.1. The diversity of percent error of the OLTARIS organ and body calculations vs. MCNP6

Male Phantoms

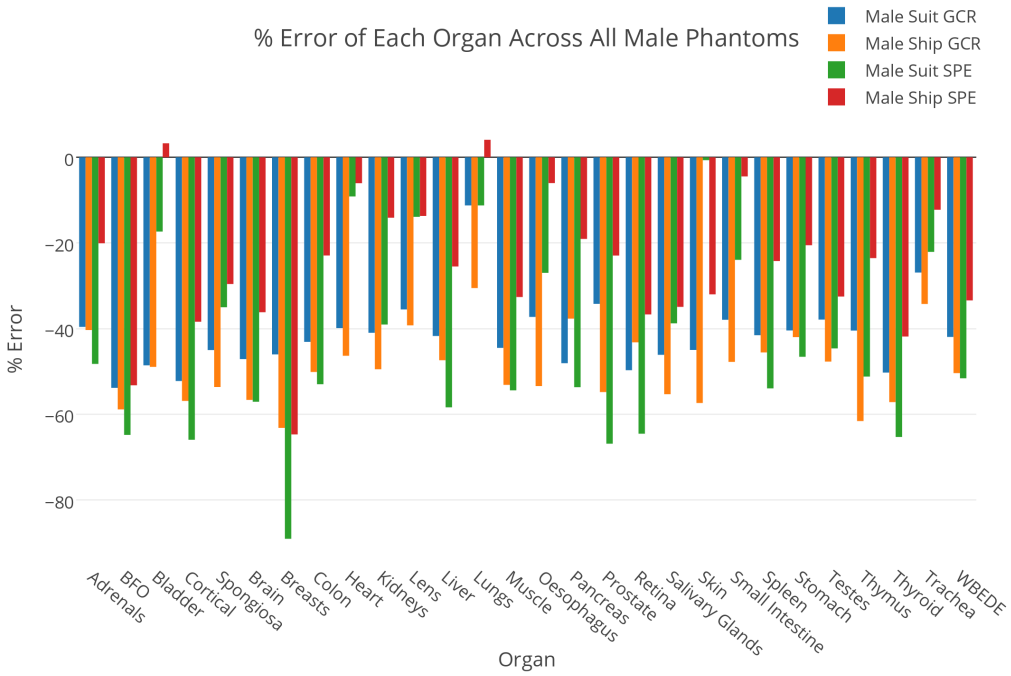

Figure 5.2. Percent error of each organ across all male phantoms

Across all male runs, the lungs and the trachea are the two organs that had relatively low percent errors regardless of shielding or radiation environment.

Female Phantoms

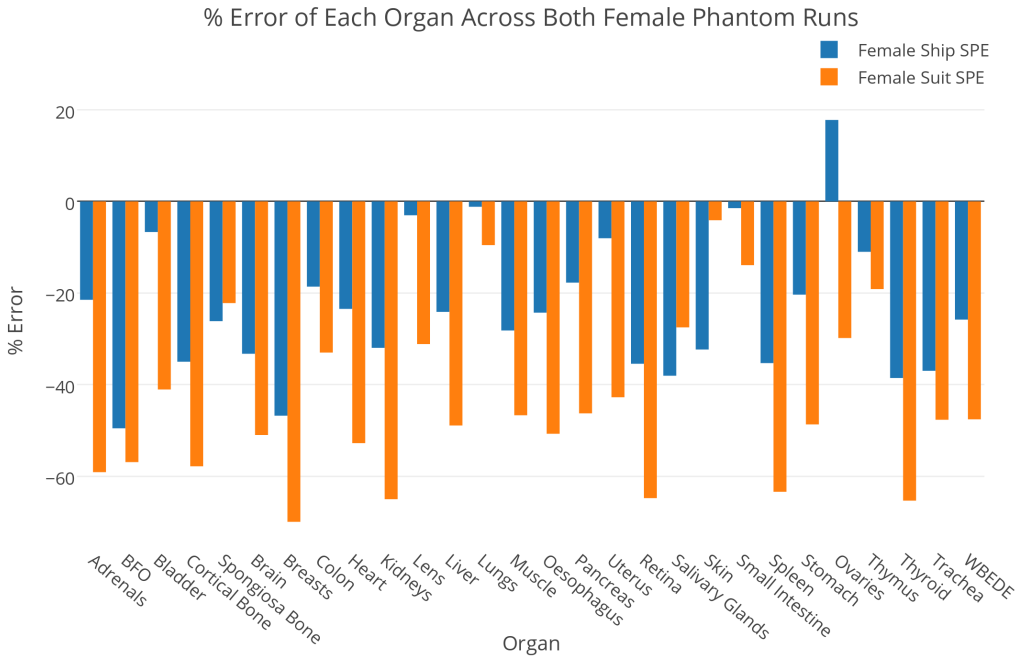

Figure 5.3. Percent error of each organ across all female phantoms

For both female runs, the lens of the eye, the lungs, the small intestine and the eyes are the four organs that had the lowest average percent error, regardless of shielding. Future research will have to determine what effect the radiation environment has on this data.

SPE Environments

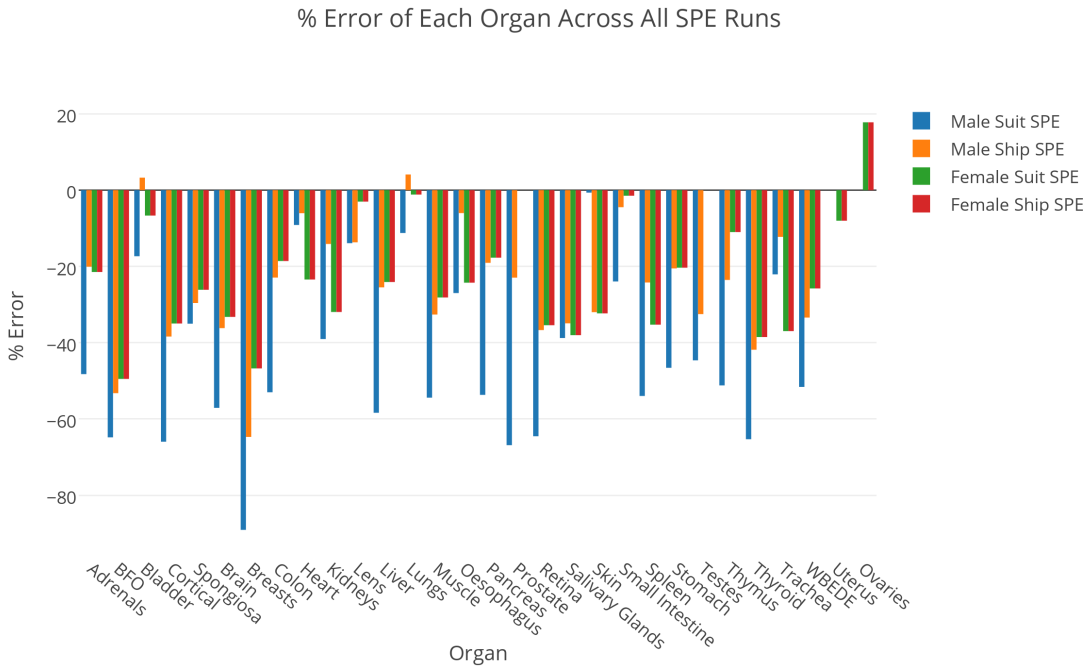

Figure 5.4. Percent error of each organ within the SPE environment

For every SPE run, the bladder, heart, small intestine, and uterus (for the female phantoms) had the lowest average percent error, regardless of phantom gender or shielding.

GCR Environments

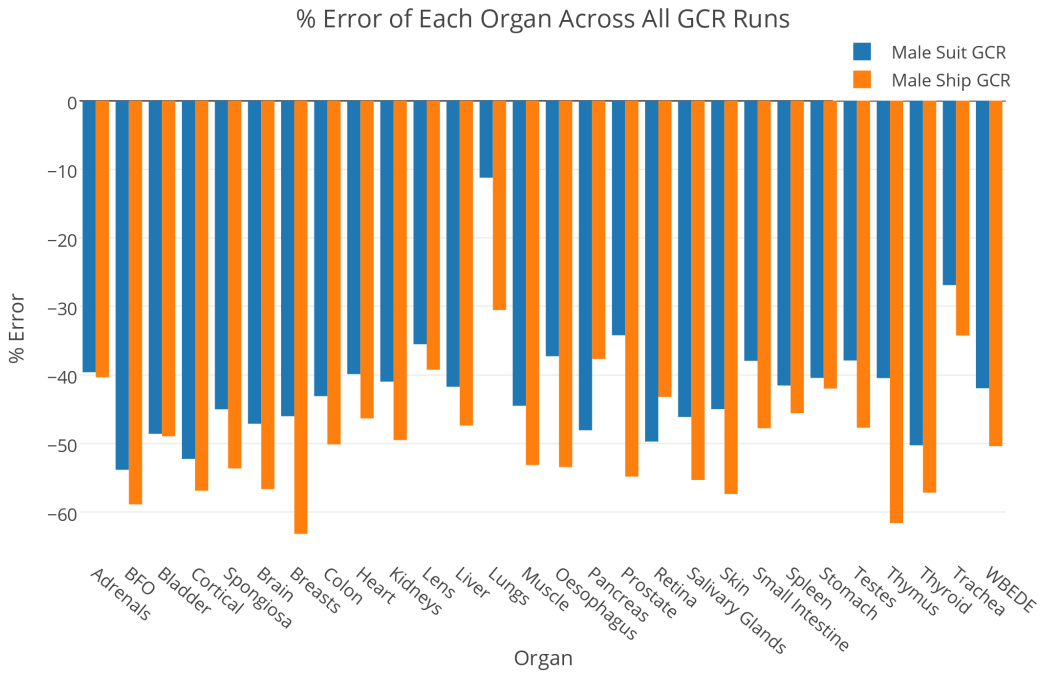

Figure 5.5. Percent error of each organ within the GCR environment

For both GCR runs, the lungs and the trachea are two organs that had relatively low percent errors, regardless of the shielding. Future research will determine if the choice of phantom has any effect on the organ data.

Thin Shielding

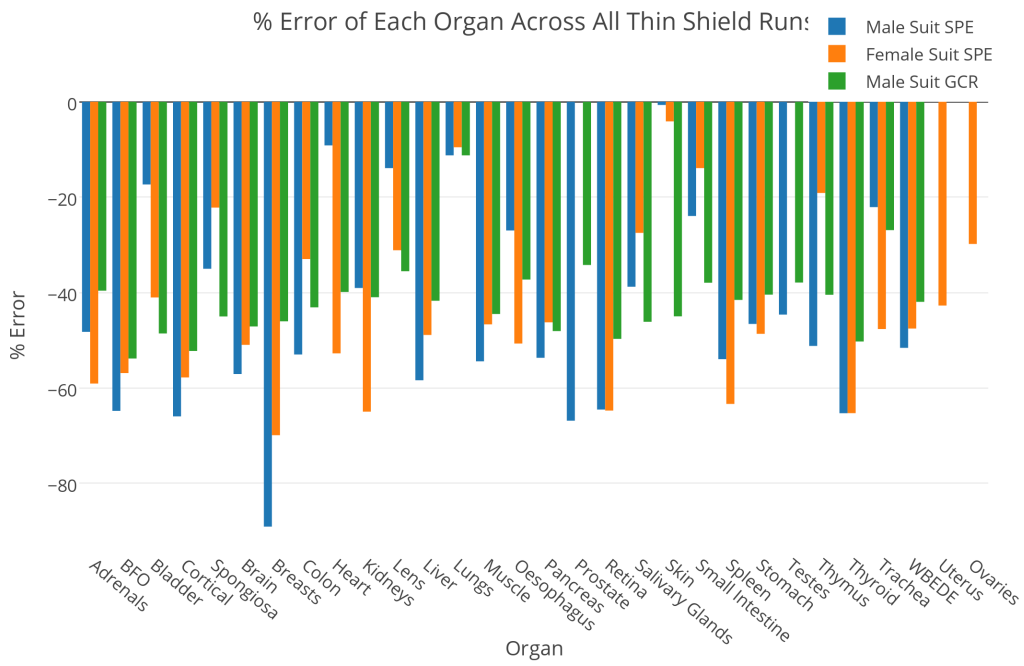

Figure 5.6. Percent error of each organ with thin shielding

For all three thin shield runs, the only organ with a consistently low percent error was the lung. The salivary glands for the male phantoms had a very low percent error, but not for the female phantom. Future research will have to confirm if this is the radiation environment or some other cause.

Thick Shielding

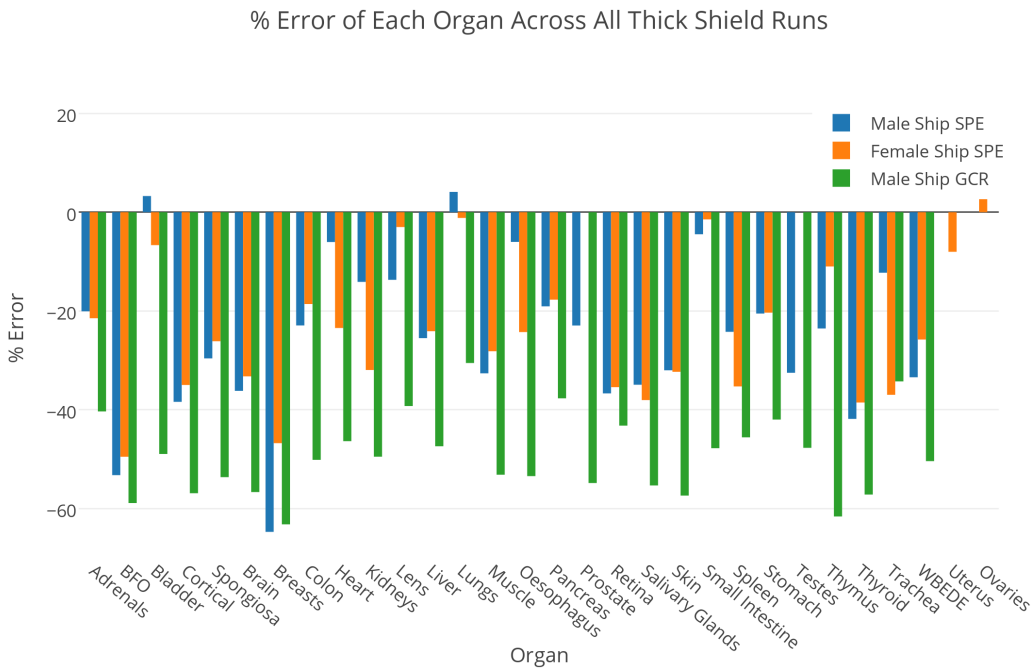

Figure 5.7. Percent error of each organ with thick shielding

For all three thick shield runs, there were no organs with a consistently low percent error across all runs. The bladder, lungs, heart, small intestine and thymus were low in error for the SPE runs, but not the GCR run; this seems to suggest that it is the radiation environment causing the most error for these particular organs.

CHAPTER 6

CONCLUSION

The combination of a Monte Carlo transport code capable of transporting the exotic particles found in space radiation with a fully-realized, voxelized human phantom, is a unique aspect of this project. Future research will expand this new capability to validate other scenarios in OLTARIS, and eventually surpass the particles transported. MCNP6 can now be used as a thorough estimate of radiation dose on a voxelized phantom, as long as the spacecraft is appropriately integrated into MCNP6.

The data discussed in Chapter 5 points to a number of interesting conclusions; there are certain environments that seem to be more favorable to accurate measurements than others (e.g., SPEs over GCRs), and certain organs are less susceptible to large errors depending on the phantom, environment, and shielding used. However, the large and nearly uniform **systemic bias** within the OLTARIS code is **between 30% and 50%** underestimation.

Since the particles transported in both codes were chosen to be identical, the remaining possible sources of systemic error from are:

- the discrepancy between MASH/FASH and the outdated phantoms MAX/FAX;
- the deterministic NUCFRG2 transport code in OLTARIS, versus the probabilistic CEM and LAQGSM event generators; and
- the approximations used in the one-dimension ``ray-tracing'' transport, versus the fully three-dimensional transport occurring in MCNP6.

The simplest of these to eliminate, ostensibly, is the upgrading of MAX and FAX in OLTARIS to the more complete MASH and FASH phantoms. The other two, however, are less simple to change, and it would be hard to untangle the proportions of error from one of these approximations compared to the other. Researchers will have to weigh the difficulty and feasibility of replacing or changing either of these approximations, more so than the update of phantoms.

Note, however, that the goal is *not* the overhaul of OLTARIS; those approximations and sources of error are the very reason OLTARIS is preferred over MCNP6: for *quick* particle transport! To this end, the paper has succeeded in identifying the magnitude of error resulting from these three approximations. Future research will help shed light on how these approximations each specifically create these errors, and then an appropriate understanding of the limitations and estimations of OLTARIS can be generalized for all researchers who use the code.

APPENDIX A

MASH and FASH Cells

Cell and Material IDs for FASH Voxels			
Cell ID	**Material ID**	**Material Density (g/cm^3)**	**Organ/Tissue**
001	44	-1.09000	Skin
002	80	-0.95000	Adipose subcutaneous
004	55	-1.05000	Eyes
005	55	-1.05000	Lens of eye
006	46	-1.05000	Muscle
007	52	-1.05000	Brain
008	86	-1.04000	Spinal cord
009	69	-1.03000	Adrenals
010	82	-0.38500	Lungs
012	50	-1.05000	Pancreas
013	48	-1.05000	Liver
014	57	-1.05000	Kidneys
015	73	-1.03000	Thymus
016	62	-1.04000	Spleen
017	85	-0.00100	Nasal passage
018	46	-1.05000	Tongue
019	85	-0.00100	Oral cavity
020	86	-1.04000	Salivary glands submandibular
021	86	-1.04000	Salivary glands parotid
022	86	-1.04000	Salivary glands sublingual
024	86	-1.04000	Pharynx + Larynx
026	71	-1.03000	Oesophagus
027	73	-1.03000	Trachea
028	64	-1.04000	Thyroid
029	86	-1.04000	Bronchi
030	83	-1.04000	Gall bladder contents
032	83	-1.04000	Stomach contents
034	83	-1.04000	Small intestine contents
036	83	-1.04000	Colon contents
038	84	-1.04000	Urinary bladder contents
039	75	-1.03000	Uterus
041	76	-1.03000	Lymphatic nodes
042	86	-1.04000	Soft tissue
043	86	-1.04000	Periarticular tissue + tendons
046	78	-1.02000	Breasts - glandular tissue
048	45	-1.06000	Blood
050	80	-0.95000	Adipose abdominal (visceral)
055	86	-1.04000	Peritoneum
089	86	-1.04000	Gall bladder wall
090	67	-1.04000	Ovaries
091	58	-1.04000	Stomach wall
093	60	-1.04000	Small intestine wall
095	60	-1.04000	Colon wall
097	65	-1.04000	Urinary bladder wall
098	80	-0.95000	Breasts adipose tissue
099	53	-1.05000	Heart wall

Cell and Material IDs for FASH Voxels (Continued)			
Cell ID	**Material ID**	**Material Density (g/cm^3)**	**Organ/Tissue**
100	1	-2.75000	Teeth
101	2	-1.92000	Mandible compact bone
102	2	-1.92000	Cranium compact bone
103	2	-1.92000	Sternum compact bone
104	2	-1.92000	Ribs compact bone
105	2	-1.92000	Clavicle left compact bone
106	2	-1.92000	Clavicle right compact bone
107	2	-1.92000	Scapula left compact bone
108	2	-1.92000	Scapula right compact bone
109	2	-1.92000	Cervical spine compact bone
110	2	-1.92000	Thorarcic spine compact bone
111	2	-1.92000	Lumbar spine compact bone
112	2	-1.92000	Sacrum compact bone
113	2	-1.92000	Pelvis compact bone
114	2	-1.92000	Humero left compact bone
115	2	-1.92000	Radius+Ulna left compact bone
116	2	-1.92000	Hand left compact bone
117	2	-1.92000	Humero right compact bone
118	2	-1.92000	Radius+Ulna right compact bone
119	2	-1.92000	Hand right compact bone
120	2	-1.92000	Femur left compact bone
121	2	-1.92000	Patela left compact bone
122	2	-1.92000	Tibia+Fibula left compact bone
123	2	-1.92000	Foot left compact bone
124	2	-1.92000	Femur right compact bone
125	2	-1.92000	Patella right compact bone
126	2	-1.92000	Tibia+Fibula right compact bone
127	2	-1.92000	Foot right compact bone
128	43	-1.10000	Hioide - compact bone
131	24	-1.18900	Mandible - spongiosa
132	14	-1.24500	Cranium - spongiosa
133	40	-1.07600	Sternum - spongiosa
134	28	-1.09200	Ribs - spongiosa
135	12	-1.19100	Clavicle (Left) - spongiosa
136	12	-1.19100	Clavicle (Right) - spongiosa
137	30	-1.12800	Scapula (left) - spongiosa
138	30	-1.12800	Scapula (Right) - spongiosa
139	32	-1.13500	Cervical spine - spongiosa
140	34	-1.08400	Thoracic spine - spongiosa
141	36	-1.17100	Lumbar spine - spongiosa
142	38	-1.05200	Sacrum - spongiosa
143	26	-1.10900	Pelvis - spongiosa
144	4	-1.18500	Humerus (Left) - spongiosa, upper part
145	8	-1.11700	Radius and Ulna (Left) - spongiosa
146	10	-1.11700	Hand (Left) - spongiosa
147	4	-1.18500	Humerus (Right) - spongiosa, upper part

Cell and Material IDs for FASH Voxels (Continued)			
Cell ID	**Material ID**	**Material Density (g/cm^3)**	**Organ/Tissue**
148	8	-1.11700	Radius and Ulna (Right) - spongiosa
149	10	-1.11700	Hand (Right) - spongiosa
150	16	-1.04600	Femur (Left) - spongiosa, upper part
151	20	-1.11700	Patella (Left) - spongiosa
152	20	-1.11700	Tibia and Fibula (Left) - spongiosa
153	22	-1.11700	Foot (Left) - spongiosa
154	16	-1.04600	Femur (Right) - spongiosa, upper part
155	20	-1.11700	Patella (Right) - spongiosa
156	20	-1.11700	Tibia and Fibula (Right) - spongiosa
157	22	-1.11700	Foot (Right) - spongiosa
161	42	-0.98000	Humerus (Left) - medullary yellow marrow
162	42	-0.98000	Radius and Ulna (Left) - medullary yellow marrow
163	42	-0.98000	Humerus (Right) - medullary yellow marrow
164	42	-0.98000	Radius and Ulna (Right) - medullary yellow marrow
165	42	-0.98000	Femur (Left) - medullary yellow marrow
166	42	-0.98000	Tibia and Fibula (Left) - medullary yellow marrow
167	42	-0.98000	Femur (Right) - medullary yellow marrow
168	42	-0.98000	Tibia and Fibula (Right) - medullary yellow marrow
170	43	-1.10000	Spine - intervertebral disks
171	43	-1.10000	Trunk - cartilage, articular
172	43	-1.10000	Neck - cartilage, thyroid and epiglot
173	43	-1.10000	Arms - cartilage, articular
174	43	-1.10000	Ribs - cartilage, articular
175	43	-1.10000	Head - cartilage, ears
176	43	-1.10000	Head - cartilage, nose
177	43	-1.10000	Legs - cartilage, articular
180	6	-1.11700	Humerus (Left) - spongiosa, lower part
182	6	-1.11700	Humerus (Right) - spongiosa, lower part
184	18	-1.11700	Femur (Left) - spongiosa, lower part
186	18	-1.11700	Femur (Right) - spongiosa, lower part
200	85	-0.00100	Air (Internal)

Cell and Material IDs for MASH Voxels			
Cell ID	**Material ID**	**Material Density (g/cm^3)**	**Organ/Tissue**
001	44	-1.09	Skin
002	79	-0.95	Adipose subcutaneous
004	54	-1.05	Eyes
005	54	-1.05	Lens of eye
006	46	-1.05	Muscle
007	51	-1.05	Brain
008	86	-1.04	Spinal cord
009	68	-1.03	Adrenals
010	81	-0.382	Lungs
012	49	-1.05	Pancreas
013	47	-1.05	Liver
014	56	-1.05	Kidneys
015	72	-1.03	Thymus
016	61	-1.04	Spleen
017	85	-0.001	Nasal passage
018	46	-1.05	Tongue
019	85	-0.001	Oral cavity
020	86	-1.04	Salivary glands submandibular
021	86	-1.04	Salivary glands parotid
022	86	-1.04	Salivary glands sublingual
024	86	-1.04	Pharynx + Larynx
026	70	-1.03	Oesophagus
027	72	-1.03	Trachea
028	63	-1.04	Thyroid
029	86	-1.04	Bronchi
030	83	-1.04	Gall bladder contents
032	83	-1.04	Stomach contents
034	83	-1.04	Small intestine contents
036	83	-1.04	Colon contents
038	84	-1.04	Urinary bladder contents
039	74	-1.03	Prostate
040	66	-1.04	Testicles
041	76	-1.03	Lymphatic nodes
042	86	-1.04	Soft tissue
043	86	-1.04	Periarticular tissue + tendons
046	77	-1.02	Glandular tissue
048	45	-1.06	Blood
049	86	-1.04	Penis
050	79	-0.95	Adipose abdominal (visceral)
055	86	-1.04	Peritoneum
089	86	-1.04	Gall bladder wall
091	58	-1.04	Stomach wall
093	59	-1.04	Small intestine wall
095	59	-1.04	Colon wall
097	65	-1.04	Urinary bladder wall
098	79	-0.95	Adipose breasts
099	53	-1.05	Heart wall

Cell and Material IDs for MASH Voxels (Continued)			
Cell ID	**Material ID**	**Material Density (g/cm^3)**	**Organ/Tissue**
100	1	-2.75	Teeth
101	2	-1.92	Mandible compact bone
102	2	-1.92	Cranium compact bone
103	2	-1.92	Sternum compact bone
104	2	-1.92	Ribs compact bone
105	2	-1.92	Clavicle left compact bone
106	2	-1.92	Clavicle right compact bone
107	2	-1.92	Scapula left compact bone
108	2	-1.92	Scapula right compact bone
109	2	-1.92	Cervical spine compact bone
110	2	-1.92	Thoracic spine compact bone
111	2	-1.92	Lumbar spine compact bone
112	2	-1.92	Sacrum compact bone
113	2	-1.92	Pelvis compact bone
114	2	-1.92	Humero left compact bone
115	2	-1.92	Radius+Ulna left compact bone
116	2	-1.92	Hand left compact bone
117	2	-1.92	Humerus right compact bone
118	2	-1.92	Radius+Ulna right compact bone
119	2	-1.92	Hand right compact bone
120	2	-1.92	Femur left compact bone
121	2	-1.92	Patella left compact bone
122	2	-1.92	Tibia+Fibula left compact bone
123	2	-1.92	Foot left compact bone
124	2	-1.92	Femur right compact bone
125	2	-1.92	Patella right compact bone
126	2	-1.92	Tibia+Fibula right compact bone
127	2	-1.92	Foot right compact bone
128	43	-1.10	Hioide compact bone
131	23	-1.228	Mandible spongiosa
132	13	-1.157	Cranium spongiosa
133	39	-1.041	Sternum spongiosa
134	27	-1.165	Ribs spongiosa
135	11	-1.151	Clavicle left spongiosa
136	11	-1.151	Clavicle right spongiosa
137	29	-1.183	Scapula left spongiosa
138	29	-1.183	Scapula right spongiosa
139	31	-1.05	Cervical spine spongiosa
140	33	-1.074	Thoracic spine spongiosa
141	35	-1.112	Lumbar spine spongiosa
142	37	-1.031	Sacrum spongiosa
143	25	-1.123	Pelvis spongiosa
144	3	-1.205	Humeri left spongiosa upper part
145	7	-1.108	Radius+Ulna left, spongiosa
146	9	-1.108	Hand left spongiosa

Cell and Material IDs for MASH Voxels (Continued)			
Cell ID	**Material ID**	**Material Density (g/cm^3)**	**Organ/Tissue**
147	3	-1.205	Humeri right spongiosa upper part
148	7	-1.108	Radius+Ulna right spongiosa
149	9	-1.108	Hand right spongiosa
150	15	-1.124	Femur left spongiosa upper part
151	19	-1.108	Patella left spongiosa
152	19	-1.108	Tibia+Fibula left spongiosa
153	21	-1.108	Foot left spongiosa
154	15	-1.124	Femur right spongiosa upper part
155	19	-1.108	Patella right spongiosa
156	19	-1.108	Tibia+Fibula right spongiosa
157	21	-1.108	Foot right spongiosa
161	41	-0.98	Humero left medullary yellow marrow
162	41	-0.98	Radius+Ulna left medullary yellow marrow
163	41	-0.98	Humero right medullary yellow marrow
164	41	-0.98	Radius+Ulna right medullary yellow marrow
165	41	-0.98	Femur left medullary yellow marrow
166	41	-0.98	Tibia+Fibula left meddullary yellow marrow
167	41	-0.98	Femur right medullary yellow marrow
168	41	-0.98	Tibia+Fibula right medullary yellow marrow
170	43	-1.1	Spine - intervertebral disks
171	43	-1.1	Trunk - cartilage articular
172	43	-1.1	Neck - cartilage thyroid and epiglot
173	43	-1.1	Arms - cartilage articular
174	43	-1.1	Ribs - cartilage articular
175	43	-1.1	Head - cartilage ears
176	43	-1.1	Head - cartilage nose
177	43	-1.1	Legs - cartilage articular
180	5	-1.108	Humero left - spongiosa lower part
182	5	-1.108	Humero right - spongiosa lower part
184	17	-1.108	Femur left - spongiosa lower part
186	17	-1.108	Femur right - spongiosa lower part
200	85	-0.001	Air internal

REFERENCES

M. Ackermann et. al. (2013). Detection of the Characteristic Pion-Decay Signature in Supernova Remnants. *Science, 339*(6121), 807-811.

Agostinelli, S., Allison, J., Amako, K. A., Apostolakis, J., Araujo, H., Arce, P., ... & Howard, A. (2003). GEANT4—a simulation toolkit. *Nuclear instruments and methods in physics research section A: Accelerators, Spectrometers, Detectors and Associated Equipment*, *506*(3), 250-303.

Allison, J., Amako, K., Apostolakis, J., Araujo, H. A. A. H., Dubois, P. A., Asai, M. A. A. M., ... & Perl, J. (2006). Geant4 developments and applications. *Nuclear Science, IEEE Transactions on*, *53*(1), 270-278.

Anderson, Herbert L. (1986). Metropolis, Monte Carlo and the MANIAC. *Los Alamos Science 14*: 96–108.

Badhwar, G. D., & O'Neill, P. M. (1994). Long-term modulation of galactic cosmic radiation and its model for space exploration. *Advances in Space Research*, *14*(10), 749-757.

Bhardwaj, A.; Gladstone, G.R. (2000). Auroral emissions of the giant planets. *Reviews of Geophysics, 38*(3), 295–353.

Bird, D.J., et. al. (1995). Detection of a cosmic ray with measured energy well beyond the expected spectral cutoff due to cosmic microwave radiation. *Astrophysical Journal*, *441*(1), 144-150.

Boetticher, H. V., Lachmund, J., Looe, H. K., Hoffmann, W., & Poppe, B. (2008). 2007 recommendations of the ICRP change basis for estimation of the effective dose: what is the impact on radiation dose assessment of patient and personnel?. *RoFo: Fortschritte auf dem Gebiete der Rontgenstrahlen und der Nuklearmedizin*, *180*(5), 391-395.

Billings, M.P., Yucker, W.R., "The Computerized Anatomical Man (CAM) Model," Summary Final Report, MDC-G4655, McDonnell Douglas Company, 1973.

Cristy, M., & Eckerman, K. F. (1987). Specific absorbed fractions of energy at various ages from internal photon sources. VI. Newborn. *ORNL/TM-8381*, *6*.

Cucinotta, F., Manuel, F., Jones, J., Iszard, G., Murrey, J., Djojonegro, B., & Wear, M. (2001). Space Radiation and Cataracts in Astronauts. *Radiation Research, 156*(5), 460-466.

Davis, J. (2008). *Fundamentals of aerospace medicine*. Philadelphia: Lippincott Williams & Wilkins.

DeWerd, L. & Kissick, M. (2014). *The phantoms of medical and health physics*. New York: Springer.

Dietze, G., Bartlett, D. T., Cool, D. A., Cucinotta, F. A., Jia, X., McAulay, I. R., ... & Sato, T. (2013). ICRP Publication 123: Assessment of Radiation Exposure of Astronauts in Space. *Annals of the ICRP*, *42*(4), 1-339.

Feldman, U.; Landi, E.; Schwadron, N. A. (2005). On the sources of fast and slow solar wind. *Journal of Geophysical Research*, 110.

Goorley, T.; James, M.; Booth, T.; Brown, F.; Bull, J.; Cox, L.J.; Durkee, J.; Elson, J.; Fensin, M.; Forster, R.A.; Hendricks, J.; Hughes, H.G.; Johns, R.; Kiedrowski, B.; Martz, R.; Mashnik, S.; McKinney, G.; Pelowitz, D.; Prael, R.; Sweezy, J.; Waters, L.; Wilcox, T.; and Zukaitis, T. "Initial MCNP 6 Release Overview", LA-UR-11-07082, Los Alamos: Los Alamos National Laboratory, also *Nuclear Technology*, 180, 298-315 (Dec 2012).

Harra, Louise; Milligan, Ryan; Fleck, Bernhard (2008). Hinode: source of the slow solar wind and superhot flares. *ESA*.

Horneck, G.; Bücker, H.; Reitz, G. (1994). Long-term survival of bacterial spores in space. *Advances in Space Research, 14*(10), 41-45.

Johnson, A. S., Badhwar, G. D., Golightly, M. J., Hardy, A. C., Konradi, A., & Yang, T. C. H. (1993). Spaceflight radiation health program at the Lyndon B. Johnson Space Center.

Kallenrode. (2004). *Space physics: an introduction to plasmas and particles in the heliosphere and magnetospheres*. Berlin New York: Springer.

Kawrakow, I. (2000). Accurate condensed history Monte Carlo simulation of electron transport. I. EGSnrc, the new EGS4 version. *Medical physics*, *27*(3), 485-498.

Kramer, R., Khoury, H. J., Vieira, J. W., Loureiro, E. C. M., Lima, V. J. M., Lima, F. R. A., & Hoff, G. (2004). All about FAX: a female adult voxel phantom for Monte Carlo calculation in radiation protection dosimetry. *Physics in medicine and biology*, *49*(23), 5203.

Kramer, R., Khoury, H. J., Vieira, J. W., & Lima, V. J. M. (2006). MAX06 and FAX06: update of two adult human phantoms for radiation protection dosimetry. *Physics in medicine and biology*, *51*(14), 3331.

Kramer, R., Cassola, V. F., Khoury, H. J., Vieira, J. W., de Melo Lima, V. J., & Brown, K. R. (2010). FASH and MASH: female and male adult human phantoms based on polygon mesh surfaces: II. Dosimetric calculations. *Physics in medicine and biology*, *55*(1), 163.

Lopez, J. & Dorso, C. (2000). *Lecture notes on phase transformations in nuclear matter*. Singapore River Edge, N.J: World Scientific.

Marsch, Eckart; Tu, Chuanyi (2005). Solar Wind Origin in Coronal Funnels. *ESA*.

Mashnik, S. G., Gudima, K. K., Prael, R. E., Sierk, A. J., Baznat, M. I., & Mokhov, N. V. (2008). CEM03. 03 and LAQGSM03. 03 event generators for the MCNP6, MCNPX, and MARS15 transport codes. *arXiv preprint arXiv:0805.0751*.

Metropolis, N.; Ulam, S. (1949). The Monte Carlo method. *Journal of the American Statistical Association 44*: 335–341.

Metropolis, N. (1987). The beginning of the Monte Carlo method. *Los Alamos Science*: 125–130

Mewaldt, R.A.; Looper, M.D.; Cohen, C.M.S.; Mason, G.M.; Haggerty, D.K.; Desaic, M.I.; Labrador, A.W.; Leskea, R.A.; Mazur; J.E. Solar-Particle Energy Spectra during the Large Events of October-November 2003 and January 2005. *29th International Cosmic Ray Conference Pune* (2005) 00, 101-104

Nelson, W. R., Hirayama, H., & Rogers, D. W. (1985). *EGS4 code system* (No. SLAC-265). Stanford Linear Accelerator Center, Menlo Park, CA (USA).

Sandridge, C.A. (2008). OLTARIS – Overview and Update on New Capabilities. *23rd Annual NASA Space Radiation Investigators' Workshop*.

Sandridge, C.A. (2014). OLTARIS – Overview and Recent Updates. *NASA Human Research Program Investigators' Workshop*.

Sandridge, C.A. (2015). OLTARIS. *OLTARIS Home Page*. Retrieved from https://oltaris.nasa.gov.

Shea, M.A.; Smart, D.F. Recent and Historical Solar Proton Events. *Radiocarbon*, *34*(2), 255-262.

Sokolov et. al. (1968). Albedo neutrons of the earth's atmosphere and their distribution in space near the earth. Canadian Journal of Physics, 1968, 46(10), 68-409.

Stabin, M.G., Watson, E.E., Cristy, M., Ryman, J.C., Eckerman, K.F. [Oak Ridge National Lab., Davis, J.L. [Tennessee Univ., … Gehlen, M.K. [San Diego State Univ. (1995). *Mathematical models and specific absorbed fractions of photon energy in the nonpregnant adult female and at the end of each trimester of pregnancy*. United States.

Suess, Steve (1999). Overview and Current Knowledge of the Solar Wind and the Corona. *The Solar Probe*. Huntsville: NASA Marshall Space Flight Center.

UNSCEAR (2008). *Sources and Effects of Ionizing Radiation.* United Nations Scientific Committee on the Effects of Atomic Radiation, 4. New York: United Nations. Retrieved 9 November 2012.

Van Allen, James A. (1958). Radiation Belts Around the Earth. *Scientific American, 200,* 39-47.

Williams, D. L. (1998). *Measurements of the isotopic composition of solar energetic particles with the MAST instrument aboard the SAMPEX spacecraft* (Doctoral dissertation, California Institute of Technology).

Wilson, J. W., Cucinotta, F. A., Tai, H., Simonsen, L. C., Shinn, J. L., Thibeault, S. A., and Kim, M. Y. (1995). *HZETRN: Description of a Free-Space Ion and Nucleon Transport and Shielding Computer Program*. NASA TP-3495. Hampton Roads: NASA Langley Research Center.

"EGSnrc: Software Tool to Model Radiation Transport." Government of Canada. National Research Council Canada. Accessed June 3, 2014.

Exec. Order No. 12196, 3 C.F.R. page 145 (1980).

"The Official FLUKA Site: FLUKA Home." The Official FLUKA Site. May 21, 2010. Accessed May 1, 2014. http://www.fluka.org/fluka.php.

"Geant4: A Toolkit for the Simulation of the Passage of Particles through Matter." Geant4. Accessed May 23, 2014. http://geant4.web.cern.ch/geant4/.

International Commission on Radiological Protection. (1991). *ICRP Publication 60: 1990 Recommendations of the International Commission on Radiological Protection* (No. 60). Elsevier Health Sciences.

NASA Space Faring – The Radiation Challenge. Module 1: Radiation. EP-2008-08-116-MSFC.

NCRP. (2000). *Radiation Protection Guidance for Activities in Low-Earth Orbit*. NCRP Report No. 132.

"PHITS Homepage." PHITS. Accessed May 20, 2014. http://phits.jaea.go.jp/.

RADAR - the RAdiation Dose Assessment Resource. Accessed March 3, 2013. http://doseinfo-radar.com/.